Optical switching in a layered altermagnet

Alessandro de Vita, Chiara Bigi, Davide Romanin, Matthew Watson, Vincent Polewczyk, Marta Zonno, François Bertran, My Bang Petersen, Federico Motti, Giovanni Vinai, et al.

▶ To cite this version:

Alessandro de Vita, Chiara Bigi, Davide Romanin, Matthew Watson, Vincent Polewczyk, et al.. Optical switching in a layered altermagnet. 2025. ⟨hal-05321440⟩

HAL Id: hal-05321440
https://hal.science/hal-05321440v1

Preprint submitted on 19 Oct 2025

Optical switching in a layered altermagnet

Alessandro De Vita***,[1,2] Chiara Bigi***,[3,*] Davide Romanin***,[4] Matthew D. Watson,[5] Vincent Polewczyk,[6] Marta Zonno,[3] François Bertran,[3] My Bang Petersen,[7] Federico Motti,[8] Giovanni Vinai,[8] Manuel Tuniz,[9] Federico Cilento,[10] Mario Cuoco,[11] Brian M. Andersen,[12] Andreas Kreisel,[12] Luciano Jacopo D'Onofrio,[11] Oliver J. Clark,[13] Mark T. Edmonds,[13] Christopher Candelora,[14] Muxian Xu,[14] Siyu Cheng,[14] Alexander LaFleur,[14] Tommaso Antonelli,[15] Giorgio Sangiovanni,[16] Lorenzo Del Re,[16] Ivana Vobornik,[8] Jun Fujii,[8] Fabio Miletto Granozio,[17] Alessia Sambri,[17] Emiliano Di Gennaro,[18] Jeppe B. Jacobsen,[19] Henrik Jacobsen,[20] Ralph Ernstorfer,[1,2] Ilija Zeljkovic,[14,†] Younghun Hwang,[21,‡] Matteo Calandra,[22,§] Jill A. Miwa,[7,¶] and Federico Mazzola[17,**]

[1]*Institut für Optik und Atomare Physik, Technische Universität Berlin,*
Straße des 17 Juni 135, 10623 Berlin, Germany

[2]*Fritz Haber Institut der Max Planck Gesellshaft,*
Faradayweg 4–6, 14195 Berlin, Germany

[3]*Synchrotron SOLEIL, F-91190 Saint-Aubin, France*

[4]*Université Paris-Saclay, CNRS, Centre de Nanosciences*
et de Nanotechnologies, 91120, Palaiseau, Paris, France

[5]*Diamond Light Source Ltd, Harwell Science and Innovation Campus,*
Didcot, OX110DE, United Kingdom

[6]*Université Paris-Saclay, UVSQ, CNRS, GEMaC, 78000, Versailles, France*

[7]*Department of Physics and Astronomy,*
Interdisciplinary Nanoscience Center,
Aarhus University, 8000 Aarhus C, Denmark

[8]*CNR-IOM Istituto Officina dei Materiali, I-34139 Trieste, Italy*

[9]*Dipartimento di Fisica, Università degli Studi di Trieste, 34127, Trieste, Italy*

[10]*Elettra - Sincrotrone Trieste S.C.p.A.,*
Strada Statale 14, km 163.5, Trieste, Italy

[11]*CNR-SPIN, c/o Universitá di Salerno, IT-84084 Fisciano (SA), Italy*

[12]*Niels Bohr Institute, University of Copenhagen, 2100 Copenhagen, Denmark*

[13]*School of Physics and Astronomy,*
Monash University, Clayton, Victoria 3800, Australia

[14] *Department of Physics, Boston College, Chestnut Hill, MA 02467, USA*
[15] *ETH Zürich, HPF E 19 Otto-Stern-Weg 1, 8093 Zürich, Switzerland*
[16] *Institute for Theoretical Physics and Astrophysics,*
University of Würzburg, D-97074 Würzburg, Germany
[17] *CNR-SPIN, c/o Complesso di Monte S. Angelo, IT-80126 Napoli, Italy*
[18] *Physics Department, University of Napoli "Federico II",*
Via Cinthia, 21, Napoli 80126, Italy
[19] *Nanoscience Center, Niels Bohr Institute,*
University of Copenhagen, 2100 Copenhagen, Denmark
[20] *European Spallation Source ERIC - Data Management*
and Software Center, 2800 Kgs. Lyngby, Denmark
[21] *Electricity and Electronics and Semiconductor Applications,*
Ulsan College, Ulsan 44610, Republic of Korea
[22] *Department of Physics, University of Trento,*
Via Sommarive 14, Povo 38123, Italy

Abstract

Altermagnetism defies conventional classifications of collinear magnetic phases, standing apart from ferromagnetism and antiferromagnetism with its unique combination of spin-dependent symmetries, net-zero magnetization, and anomalous Hall transport [1–6]. Although altermagnetic states have been realized experimentally [7, 8], their integration into functional devices has been hindered by the structural rigidity and poor tunability of existing materials [9–11]. First, through cobalt intercalation of the superconducting 2H-NbSe$_2$ polymorph, we induce and stabilize a robust altermagnetic phase and using both theory and experiment, we directly observe the lifting of Kramers degeneracy [12–15]. Then, using ultrafast laser pulses, we demonstrate how the low temperature phase of this system can be quenched, realizing the first example of an optical altermagnetic switch. While shedding light on overlooked aspects of altermagnetism, our findings open pathways to spin-based technologies and lay a foundation for advancing the emerging field of altertronics [16, 17].

*** These authors contributed equally.

Altermagnetism, recognized as the third elementary type in the classification of non-relativistic spin-group symmetries, is defined by the coexistence of zero-net magnetization and the lifting of Kramers degeneracies, which lead to distinctive transport phenomena [2, 18–20]. These degeneracies are shaped by opposite spin sublattices, interconnected through rotational symmetry in real space [1, 7]. Distinct from both ferromagnetism and antiferromagnetism, this newly identified phase has sparked considerable interest, presenting new challenges for the development of spin-based technologies with potentially groundbreaking properties. The absence of net magnetization offers an advantage over conventional ferromagnetic technologies by mitigating stray magnetic fields. Simultaneously, the lifting of spin degeneracies, coupled with momentum-dependent spin-locking, facilitates efficient spin-filtering. Moreover, contrary to traditional collinear antiferromagnets, altermagnets intrinsically break time-reversal symmetry, giving rise to phenomena such as the anomalous Hall effect, highlighting their potential for novel electronic applications [9–11, 21].

---

[*] chiara.bigi@synchrotron-soleil.fr

[†] ilija.zeljkovic@bc.edu

[‡] younghh@uc.ac.kr

[§] m.calandrabuonaura@unitn.it

[¶] miwa@phys.au.dk

[**] federico.mazzola@spin.cnr.it

This rapidly evolving field presents compelling opportunities to extend this phenomenology to two dimensional (2D) material systems [22, 23]. 2D and thin-film altermagnets, along with their layered analogues, are particularly intriguing, envisioned as altermagnetic counterparts to graphene and graphite. [24]. While significant progress has been made, the high symmetry of most 2D antiferromagnets prevents the stabilization of the altermagnetic phase [25–27] and scalable layer-by-layer synthesis methods remain scarce [28], highlighting the need for innovative approaches. Building on proposed material growth strategies [24], we tune the superconducting polymorph 2H-$NbSe_2$ via site-ordered Co intercalation, stabilizing a robust and well-defined altermagnetic state. Using a combined theoretical and experimental approach, we demonstrate its magnetism, altermagnetic band splitting, and spin texture, establishing $Co_{1/4}NbSe_2$ as the first g-wave altermagnetic layered material. Finally, we show how to control the low-temperature phase of this layered altermagnet by using ultrafast laser pulses.

Single crystals of $Co_{1/4}NbSe_2$ were synthesized using the chemical vapour transport (CVT) method. Their composition and phase were monitored respectively by X-ray photoelectron spectroscopy (XPS) and X-ray diffraction (XRD). (For further details, refer to the Methods Section and the Supplementary Information Figs. S1–S3.) Consistent with Ref. [24], the crystal structure depicted in Fig. 1a reveals Co-intercalated $NbSe_2$ planes, which doubles the unit cell of the system, giving a 2×2 modulation, which we detect by low-energy electron diffraction (LEED) at low temperature (see Fig. 1b). However, while the doubling of the unit cell is an intrinsic feature of the crystal structure, we also observe, by spectroscopy, a reduction of the $2{\times}2$ modulation above 150 K (See Supplementary Information Fig. S7), possibly attributable to the occurrence of an additional charge order (See Supplementary Information Figs. S4—S6 for time-resolved optical spectroscopy measurements).

Similar to other intercalated transition metal dichalcogenides (TMDs) [29], $Co_{1/4}NbSe_2$ cleaves to reveal two distinct surface terminations, each displaying markedly different electronic properties. Figs. 1c–1d present schematics of these two terminations, which were experimentally distinguished using scanning tunneling microscopy (STM). The Se-terminated surface, which appears to be the cleanest, exhibits the characteristic triangular tiling of the 2H-$NbSe_2$ polymorph (Fig. 1e). In contrast, the Co-terminated surface is typically more disordered yet remains clearly distinguishable from the Se-terminated surface (Fig. 1f). Additional STM data are provided in Supplementary Information Fig. S2.

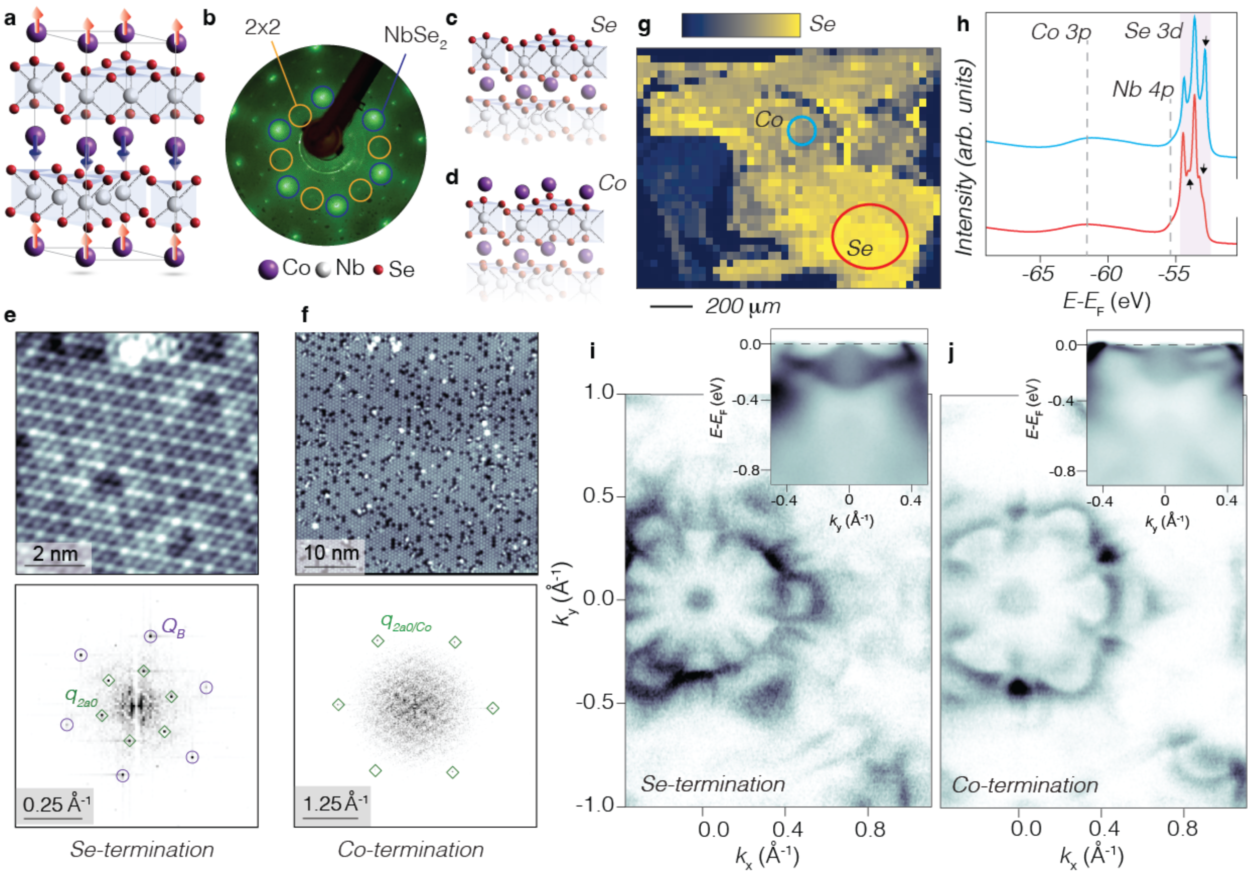

FIG. 1. **Surface-dependent crystalline and electronic structure.** **a.** Schematic of $Co_{1/4}NbSe_2$ formed by 2H-$NbSe_2$ planes linked by Co atoms in a 2×2 reconstruction. **b.** LEED data (145 eV, 10K) showing the reconstruction: the orange circles indicate the 2×2 features, while the blue circles are the primitive ones. **c–d.** Schematics showing the possible surface terminations after cleaving: Se and Co. These two terminations are clearly visible in both STM and micro-ARPES data. **e.** Se-termination (characterized by the triangular tiling) and **f.** Co-termination, measured by STM, and their corresponding Fourier transforms. **g.** micro-ARPES spatial map acquired by measuring the Se $3d$ and Co $3p$ core levels with yellow corresponding to Se-terminated regions. **h.** Core levels acquired from the two different surface terminations (curve colours matching the circle colours in **g**); the highlighted spectral features are attributed to surface replicas for the Se-termination. **i–j.** Corresponding Fermi surfaces and (E, k) dispersions, collected at 25 K with p-polarized photons at 47.5 eV (black indicates high intensity in the ARPES scale).

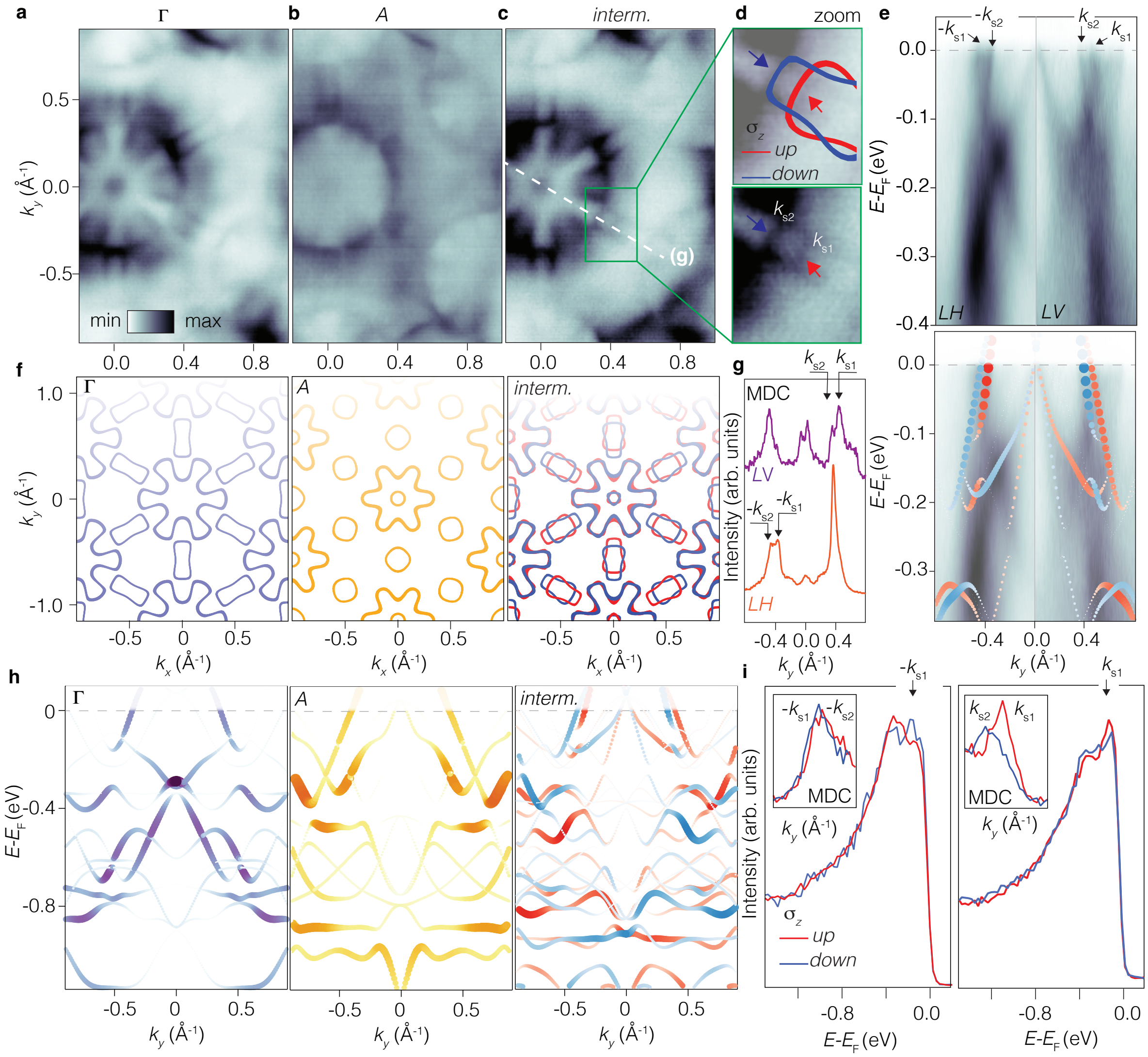

FIG. 2. **Fermiology, DFT, and spin splitting.** Fermi surfaces at bulk Γ (51 eV, **a.**), A (75 eV, **b.**), and an intermediate point near $k_z = 0.25$ Å^{-1} (55 eV, **c.** - this energy makes the matrix elements favorable to detect the splitting in the Fermi surface). **d.** Zoom-in on the splitting, with and without DFT calculations. The arrows indicate sections were the bands are prominently separated. **e.** (E, k)-spectra at an intermediate point between Γ and A (44 eV shows more favorable matrix elements in this direction - See Supplementary Information for additional energies) using p- (LH, left) and s-polarized (LV, right) light, with DFT calculations on the lower panel.**f.** DFT spin-polarized 2D Fermi surfaces of Co$_{1/4}$NbSe$_2$ at $k_z = 0$ Å^{-1} , $k_z = 0.5$ Å^{-1} , and $k_z = 0.25$ Å^{-1} **g.** MDCs at the Fermi level from **e.**, confirming multiple split bands. **h.** DFT spin-polarized bands of Co$_{1/4}$NbSe$_2$ unfolded in the large Brillouin zone of (1×1) NbSe$_2$ along $\mathrm{M} - \Gamma - \mathrm{M}$ for $k_z = 0$ Å^{-1} , 0.5 Å^{-1} , and 0.25 Å^{-1} , with spectral weight $P_{\vec{K}m}$. **i.** spin-ARPES at opposite k-points (55 eV, as in **c.**), showing EDCs at k_{s1} and MDCs at the Fermi level (insets).

Spectroscopically, our data analysis reveals multiple splittings in the electronic band structure and suggests a need to revisit earlier interpretations and the inferred determination of altermagnetic splittings [30]. We used angle-resolved photoelectron spectroscopy with few-micron spatial resolution (micro-ARPES) to validate these observations. Fermi surfaces for each surface termination were acquired by mapping the sample's surface composition through Se $3d$ and Co $3p$ core level measurements (Fig. 1g). This approach allowed accurate positioning of the light spot on either Se- or Co-terminations. The Se-termination, which seems dominant in this sample, exhibits surface replicas of the $3d$ core levels (red curve), while Co-terminated regions show distinct spectral features, including an additional peak at lower energies (blue curve) possibly formed by a different coordination of Co-Se atoms; see Fig. 1h.

The energy and momentum (E, k) dispersions along the $\Gamma - \mathrm{M}$ direction, along with the Fermi surface maps, reveal a complex and rich electronic structure. For both terminations, the intensity displays a pronounced threefold symmetry, accompanied by multiple petals and back-folded features. As shown in Supplementary Information Fig. S7 and S9, the in-plane back-folding results from the 2×2 modulation, which becomes significantly weaker above 150 K. This modulation is evidenced by the replication of Γ-point features at the M-point. The Se-termination is overall the most prevalent and dominates high-resolution ARPES measurements with larger light spot sizes, as seen in the Supplementary Information Figs. S7-S12. We accordingly restrict our analysis to data obtained from this termination; other surface-specific phenomena will be the focus of a separate study.

From a recent comprehensive classification of space groups and their associated allowed altermagnetic spin-splittings [31], it follows that 2×2 reconstructed $\mathrm{Co}_{1/4}\mathrm{NbSe}_2$ (SG 194) must feature g-wave altermagnetic spin-split bands of the generic form $k_z k_y\ (3k_x^2 - k_y^2)$. Thus, in this g-wave altermagnet, the role of k_z is pivotal: the breakdown of Kramers degeneracy manifests in the electronic structure away from bulk high-symmetry points. Accurately resolving these altermagnetic features, within the Brillouin zone, requires high-resolution photon energy dependent measurements to control k_z. The small step size in photon energy is not merely advantageous but essential in identifying altermagnetic features. The large c-axis lattice constant of $\mathrm{Co}_{1/4}\mathrm{NbSe}_2$ (see Supplementary Information Fig. S1 and discussion) means each photon energy probes multiple k_z values simultaneously, leading to partial spectral broadening [32]. Nevertheless, varying photon energy enables modulation of

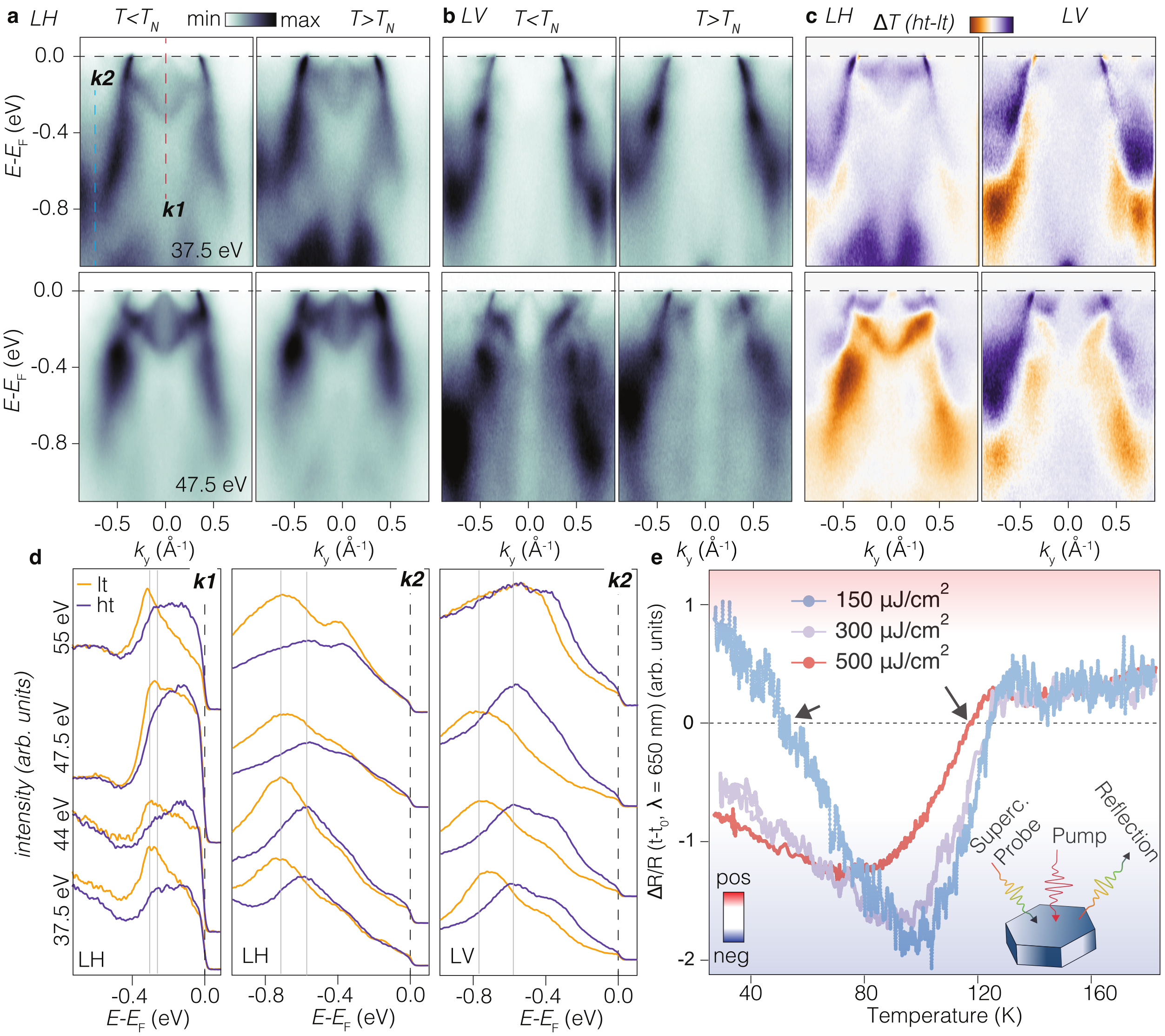

FIG. 3. **Control of the altermagnetic phase.** ARPES spectra (black indicates high intensity in the ARPES scale) collected at two distinct photon energies: 37.5 eV (top row) and 47.5 eV (bottom row), and for temperatures above and below T_N. These are shown for both **a.** p-polarization (LH) and **b.** s-polarization (LV). **c.** The difference between spectra collected above and below T_N; orange (purple) corresponds to a negative (positive) difference. The strong electronic renormalization, indicating a transition, manifests as a decrease in the overall bandwidth, while k_F remains constant. **d.** EDCs collected at different photon energies (indicated along the vertical axis) for spectra below T_N (orange) and above it (purple). These are shown for two k values (*k1* and *k2*) as indicated in **a.** **e.** Optical control of the altermagnetic phase. By increasing the pump excitation fluence, the sign change of the ΔR signal located at 50 K for 150 µJ cm^{-2} is quenched. The curves have been normalized to the absorbed fluence.

matrix elements and band intensities, which significantly enhances the detection of subtle spectral features. Such features are shown in white-black color scale, where black indicates the presence of electrons. This capability is exemplified in the Fermi surface maps obtained at different photon energies (Fig. 2a–c; see also Supplementary Information Figs. S10–S12). Despite k_z-broadening effects, these maps probe distinct k_z planes, corresponding to bulk Γ, A, and an intermediate point near $k_z = 0.25\,\text{Å}^{-1}$, where altermagnetic features appear pronounced. While all Fermi surfaces share common features, *i.e.* hexagonal flower-like central contours and elongated 'spindles', the map in Fig. 2c reveals a clear splitting of the bands, a feature that eluded detection in prior studies (see arrows pointing at flat portions of the Fermi contours where the separation is more prominent in Fig. 2d). These splittings are also visible in the (E, k) spectra (Fig. 2e) and their momentum distribution curves (MDCs) extracted at the Fermi level (Fig. 2g). We note that in the Fermi surfaces, some of the spectral features appear as filled patches of intensity rather than contours as expected from density functional theory (DFT) calculations. This is attributable to photoemission matrix elements, which, as one can see from Fig. 2, strongly vary with both geometry and photon energy.

The experimental Fermi surfaces align with DFT (Fig. 2f and Fig. S16) in capturing the fermiology across the k_z planes. The spin-splitting of the Kramers-paired bands at multiple momenta show remarkable agreement. This agreement is highlighted in Fig. 2d, where the spin-up (red) and spin-down (blue) bands from the DFT calculations coincide exactly with the experimental data. There is a similarly strong match between the DFT calculated (E, k) distributions across different k_z values and acquired micro-ARPES data, as shown in Fig. 2h, where blue and orange curves correspond to Γ- and A-points, respectively (see also Supplementary Information Fig. S13 for DFT-calculated (E, k) spectra in the $\Gamma - \mathrm{K}$ direction). In order to display a simpler representation of the electronic dispersion for comparison with micro-ARPES measurements, we have mapped the spin-polarized electronic eigenvalues and eigenvectors of the bulk altermagnetic 2×2 $\mathrm{Co_{1/4}NbSe_2}$ supercell (SC) into the bigger Brillouin zone of the 1×1 $\mathrm{NbSe_2}$ primitive cell (PC) via an unfolding scheme [33]. The thickness of the bands in the unfolded electronic dispersions is proportional to the spectral weight:

$$P_{\vec{K}m}(\vec{k}_i) = \sum_n \left| \left\langle \vec{K}m \middle| \vec{k}_i n \right\rangle \right|^2, \tag{1}$$

which is the probability of finding a set of PC states, $\left|\vec{k}_i n\right\rangle$, contributing to the SC state, $\left|\vec{K}m\right\rangle$ [33], where m and n are band indices and i runs over the number of $\vec{K}$ vectors.

Notably, while eigenvalues for $k_z = 0$ and $k_z = 0.50$ are spin-degenerate (as expected for an antiferromagnetic system), DFT results for $k_z = 0.25$ (Fig. 2h, where the red/blue colors are used to highlight spin-up/down bands) provide a precise benchmark for identifying where Kramers degeneracies are lifted, enabling a one-to-one correspondence with the experimental data. Near the Fermi level, the theoretical altermagnetic splitting is in excellent agreement with the experimental spectra (Fig. 2e), and the bands forming the altermagnetic pairs are labeled as $\pm k_{s1,s2}$. The non-zero spin character of these bands is further validated by spin-ARPES measurements (Fig. 2i), collected for the σ_z spin-component at multiple k values within the plane centered at $k_z = 0.25$. Both energy distribution curves (EDCs) at $\pm k_{s1}$ and MDCs at the Fermi level across numerous k points reveal a small, yet clear, spin-reversal pattern. This behavior is consistent with theoretical predictions and is observed at four different k points in the MDCs (insets of Fig. 2i), further supporting the validity of our findings.

Altermagnetism in some compounds has been recently established, yet controlling this phase remains a formidable challenge [16]. Temperature is a natural tuning parameter for altermagnetic behaviour. Dale et al. analyzed the temperature dependence of $\mathrm{Co}_{1/4}\mathrm{NbSe}_2$ and reported notable changes in the MDC extracted at the Fermi level [30]. In agreement with Dale et al., we observe a similar behavior; see, for example, Fig. 3a for bands acquired at 47.5 eV. Our study also reveals a pronounced band renormalization when crossing the Néel temperature T_N, as shown in Fig. 3a–d (see also Supplementary Information Fig. S8). This renormalization, observable across multiple photon energies and independent of light polarization, indicates that while the Fermi wavevector k_F remains constant, thus no change in the electron count is observed, the electronic bandwidth decreases significantly as the system transitions from 20 K ($T < T_N$) to 70 K ($T > T_N$). This effect is particularly evident in Fig. 3c–d. Fig. 3c displays the difference in spectral intensity between data collected above and below T_N, highlighting the redistribution of spectral weight. Orange color denotes predominant low temperature features, while purple color is used for high temperature. Fig. 3d shows EDCs extracted at specific k points (indicated in Fig. 3a) across various photon energies. This observation underscores a strong modulation of spectral weight accompanying the low temperature transition. Crucially, micro-ARPES provides precise spatial control, allowing us to control and check the micron-sized sample position across all temperatures. These changes, which are both partially similar to but also additional to those observed in Ref. [30], become visible at a temperature as low as 70 K, suggesting that the transition temperature in this material may be lower than previously reported. Furthermore, in Supplementary Information Fig. S7, we report that at 155 K there is negligible 2×2 band folding, suggesting that the high-temperature transition might be linked to charge order effects different from magnetism.

While temperature control is an expected lever for probing altermagnetic phases, we also demonstrate an optical mechanism to quench the low-temperature phase transition, achieving a fluence-dependent control by means of an ultrashort laser pulse. Fig. 3e shows the evolution of the reflectivity variation ($\Delta R/R$) measured immediately after the absorption of the ultrashort pump pulse ($t \sim t_0$). At a fluence of approximately 150 μJ cm^{-2}, we observe two sign changes in $\Delta R/R$, occurring near 130 K and 50 K. These temperatures correspond to the 2×2 ordering and the low-temperature transition in the resistivity (Supplementary Information Fig. S1c), respectively, suggesting a link between the sign of $\Delta R/R$ and specific phases of $Co_{1/4}NbSe_2$. By increasing the fluence to $\sim$ 300 μJ cm^{-2} we observe the sign change at 50 K disappears, *i.e.* the low-temperature phase is quenched. Further increasing the fluence to $\sim$ 500 μJ cm^{-2} shifts the sign change at 130 K to lower temperatures, suggesting that the 2×2 modulation is also strongly perturbed at this fluence. Importantly, we estimate that at the highest fluence the continuous laser heating remains below 5 K, ruling out lattice average heating effects as the origin of the observed ΔR changes. Given the short timescale at which the sign change is observed, the quenching of the low-temperature phase is likely to have an electronic origin. By demonstrating the first example of optical control of the phase diagram in a layered altermagnet, we open pathways for ultrafast, energy-efficient manipulation in altermagnetic materials [34].

Open questions remain regarding the transition temperature observed in our study compared to previous observations. For instance, Refs. [24, 30] attribute the Néel temperature to a higher value; we identify it as a structural transition temperature, consistent with both reflectivity and diffraction measurements. In contrast, the low-temperature transitions observed in Ref. [30] from 30 K to 40 K were attributed to a charge-density wave (CDW), similar to that in the parent compound $NbSe_2$, which occurs near comparable temperatures [35, 36]. However, Mandujano et al. have recently proposed that Co intercalation in $NbSe_2$ suppresses the bulk pristine CDW [37], and indeed we observe no evidence of its presence in the electron-phonon coupling oscillations in our data; see Supplementary Information Figs. S4-S6. Instead, our results suggest a magnetic phase transition as the more plausible interpretation. Despite this, our investigation clearly demonstrates altermagnetism in this compound, with unquestionable agreement between theory and experiment.

In conclusion, we have demonstrated the realization and control of altermagnetism in the layered g-wave system $Co_{1/4}NbSe_2$, stabilized via Co intercalation in 2H-$NbSe_2$. Using micro-ARPES, spin-ARPES, and temperature-dependent reflectivity combined with DFT, we provide direct evidence of Kramers degeneracy lifting and reveal the spin-polarized band splitting characteristic of altermagnetic phenomena, including temperature-driven band renormalization. Importantly, we introduce optical pumping as a novel mechanism to control phase transitions in a layered altermagnet, achieving an optical switch independent of thermal effects. By simply modulating the laser fluence, we control reflectivity and suppress low-temperature transitions, offering a pathway to ultrafast, energy-efficient spin technologies. These findings establish $Co_{1/4}NbSe_2$ as a model system for layered altermagnets and highlight optical control as a foundation for advancing spin-based information processing and altertronics.

Acknowledgements

F.M. greatly acknowledges the NFFA-DI funded by the European Union – NextGenerationEU, M4C2, within the PNRR project NFFA-DI, CUP B53C22004310006, IR0000015. D.R. acknowledges support from the HPC resources of IDRIS, CINES, and TGCC under Allocation No. 2024-A0160914101 made by GENCI. M.B.P. and J.A.M gratefully acknowledge support from DanScatt (7129-00018B). M.C. acknowledges the European Union (ERC, DELIGHT, 101052708). I.Z. gratefully acknowledges the support from the US Department of Energy grant number DE-SC0025005. We thank A. Jones for his support during measurements at the SGM4 beamline. This work was partially performed in the framework of the Nanoscience Foundry and Fine Analysis (NFFA-MUR Italy Progetti Internazionali) project (www.trieste.NFFA.eu). F. Motti acknowledges the support of the EC project SINFONIA (H2020-FET-OPEN-964396). A.D.V. acknowledges support from the Max Planck

Society, the European Research Council (ERC) under the European Union's Horizon 2020 research and innovation program (Grant No. ERC-2015-CoG-682843), and the SFB/TRR 227 "Ultrafast Spin Dynamics".

Methods

Sample Growth

Single crystals of $Co_{1/4}NbSe_2$ were synthesized using the chemical vapor transport (CVT) method. High-purity cobalt (Co, 99.99%), niobium (Nb, 99.999%), and selenium (Se, 99.9999%) powders served as starting materials. To prevent contamination and residual oxygen during synthesis, the quartz ampoule was chemically cleaned and subjected to vacuum heat treatment prior to loading. The raw materials were then sealed in a quartz ampoule (approximately 10 mm in diameter and 150 mm in length) along with iodine (5 mg/cm^3 relative to ampoule volume) as the transport agent. The sealed ampoule was evacuated to a high vacuum and placed in a two-zone horizontal furnace, with the source region maintained at a higher temperature than the growth region. Optimal temperature gradients and iodine concentration were critical for achieving high-quality crystal growth. For $Co_{1/4}NbSe_2$, the source region was held at 960–980 °C, while the growth region temperature was initially increased incrementally from 880 °C to 900 °C over 100 hours. Subsequently, both zones were held at constant temperatures for an additional 300 hours to facilitate the growth of large single crystals. Finally, the temperature was reduced gradually over 100 hours, with the source region cooled to 200 °C and the growth region to 100 °C, before allowing the ampoule to cool naturally to room temperature. The resulting single crystals measured approximately $5 \times 5 \times 0.1\,\mathrm{mm}^3$. Residual iodine was removed from the crystals by rinsing with a methanol solution. The mole fraction 'x' in Co_xNbSe_2 was preliminarily determined using energy-dispersive x-ray spectroscopy (EDS) in a field-emission scanning electron microscope (FE-SEM, JEOL 7500). High-precision quantification was subsequently performed using x-ray photoelectron spectroscopy (XPS) at the APE-HE beamline of the Elettra synchrotron radiation facility in Trieste, Italy (details in Supplementary Information). The crystal structure and quality were confirmed using high-resolution x-ray diffraction (XRD, D8 Advance, Bruker, Germany). Additional sample characterization is shown in the Supplementary Information.

Synchrotron radiation measurements

micro-ARPES measurements were performed on in situ cleaved samples. The beam was focused using the capillary mirror optic at the I05 beamline at Diamond Light Source, with a final beam spot of ∼ 4 µm FWHM. The base sample temperature was 25 K. The standard ARPES data were acquired at the CASSIOPEE beamline at Synchrotron SOLEIL (Paris, France) with momentum and energy resolutions better than $0.018\,\text{Å}^{-1}$ and 10 meV, respectively. The sample temperature was fixed at circa 20 K, *i.e.* well below the magnetic transition temperature, for all measurements. The Fermi surfaces were obtained by rotating the sample around the analyzer focus, with the slit positioned orthogonal to the rotation axis. Data were acquired using photon energies in the range from 25 eV to 75 eV, methodology valuable for analyzing spectral features and precisely determining k_z across the Brillouin zone. Spin-ARPES was performed using V-LEED technology at the APE-LE laboratory at the Elettra Synchrotron (Trieste, Italy) and with LH light. For these measurements, the samples were aligned with the slit along the $\Gamma - \text{M}$ direction and kept under normal emission conditions. The various momenta were reached via use of deflectors. The spin-ARPES was performed with the sample held at a temperature of 15 K. In all ARPES and spin-ARPES measurements, the samples were fixed to the sample holder using silver epoxy (HD20E, Epotek). A small ceramic post was secured to the top of the sample using the same epoxy. Once the samples were introduced into the measurement chamber, they were cleaved under ultrahigh vacuum conditions (better than 1×10^{-10} mbar) and after being cooled at the base temperature of 15 K.

Computational details

Collinear spin-polarized DFT calculations have been performed using the plane-wave pseudopotential method as implemented in the Quantum ESPRESSO package [38, 39]. We employed a norm-conserving pseudopotential for Se atoms and ultrasoft pseudopotentials for Nb and Co atoms, with an energy cut-off of 45 Ry and 450 Ry for the wave-function and elctron density respectively. Electronic band structure and energetics have been obtained through Perdew-Burke-Ernzerhof (PBE) [40] exchange-correlation functional. The Brillouin zone has been sampled with a k-vector mesh of $9 \times 9 \times 16$ points and a first-order Methfessel-Paxton [41] electronic smearing of 5 mRy, assuring convergence of the total energy per atom in the supercell. We investigated the energetics of Co-intercalated 2×2 NbSe_2 ($\text{Co}_{1/4}\text{NbSe}_2$) in the paramagnetic (PM), ferromagnetic (FM) and altermagnetic (ALM) configuration and as a function of the Co position (see Supplementary Information, Section VI). Electronic dispersions at different k_z of the most stable ALM $Co_{1/4}NbSe_2$ structure have then been mapped into the large Brillouin zone of 1×1 $NbSe_2$ via an unfolding procedure [33] implemented in the code unfold.x [42].

Extended data is available for this paper at https://xxxx

Supplementary Information The online version contains Supplementary Information available at https://xxx

Data availability The data that support the findings of this study are available from the corresponding authors upon reasonable request.

Code availability The code that support the findings of the study is available from the corresponding authors on reasonable request.

Correspondence and requests for materials should be addressed to .

Competing financial interests

The authors declare no competing financial interests.

---

[1] L. Šmejkal, J. Sinova, and T. Jungwirth, Beyond conventional ferromagnetism and antiferromagnetism: A phase with nonrelativistic spin and crystal rotation symmetry, Phys. Rev. X **12**, 031042 (2022).

[2] L. Šmejkal, J. Sinova, and T. Jungwirth, Emerging research landscape of altermagnetism, Phys. Rev. X **12**, 040501 (2022).

[3] L. Bai, W. Feng, S. Liu, L. Šmejkal, Y. Mokrousov, and Y. Yao, Altermagnetism: Exploring new frontiers in magnetism and spintronics, Advanced Functional Materials **34**, 2409327 (2024).

[4] T. A. Maier and S. Okamoto, Weak-coupling theory of neutron scattering as a probe of altermagnetism, Phys. Rev. B **108**, L100402 (2023).

[5] T. Jungwirth, R. M. Fernandes, J. Sinova, and L. Smejkal, Altermagnets and beyond: Nodal magnetically-ordered phases (2024), arXiv:2409.10034 [cond-mat.mtrl-sci].

[6] C. Song, H. Bai, Z. Zhou, L. Han, H. Reichlova, J. Dil, J. Liu, X. Chen, and F. Pan, Observation of a spontaneous anomalous hall response in the Mn_5Si_3 d-wave altermagnet candidate, Nat. Rev. Mater. 10.1038/s41578-025-00779-1 (2025).

[7] J. Krempaský, L. Šmejkal, S. W. D'Souza, M. Hajlaoui, G. Springholz, K. Uhlířová, F. Alarab,

P. C. Constantinou, V. Strocov, D. Usanov, W. R. Pudelko, R. González-Hernández, A. Birk Hellenes, Z. Jansa, H. Reichlová, Z. Šobáň, R. D. Gonzalez Betancourt, P. Wadley, J. Sinova, D. Kriegner, J. Minár, J. H. Dil, and T. Jungwirth, Altermagnetic lifting of Kramers spin degeneracy, Nature **626**, 517 (2024).

[8] S. Reimers, L. Odenbreit, L. Šmejkal, V. N. Strocov, P. Constantinou, A. B. Hellenes, R. Jaeschke Ubiergo, W. H. Campos, V. K. Bharadwaj, A. Chakraborty, T. Denneulin, W. Shi, R. E. Dunin-Borkowski, S. Das, M. Kläui, J. Sinova, and M. Jourdan, Direct observation of altermagnetic band splitting in CrSb thin films, Nature Communications **15**, 2116 (2024).

[9] Z. Feng, X. Zhou, L. Šmejkal, L. Wu, Z. Zhu, H. Guo, R. González-Hernández, X. Wang, H. Yan, P. Qin, X. Zhang, H. Wu, H. Chen, Z. Meng, L. Liu, Z. Xia, J. Sinova, T. Jungwirth, and Z. Liu, An anomalous Hall effect in altermagnetic ruthenium dioxide, Nature Electronics **5**, 735 (2022).

[10] R. D. Gonzalez Betancourt, J. Zubáč, R. Gonzalez-Hernandez, K. Geishendorf, Z. Šobáň, G. Springholz, K. Olejník, L. Šmejkal, J. Sinova, T. Jungwirth, S. T. B. Goennenwein, A. Thomas, H. Reichlová, J. Železný, and D. Kriegner, Spontaneous anomalous Hall effect arising from an unconventional compensated magnetic phase in a semiconductor, Phys. Rev. Lett. **130**, 036702 (2023).

[11] O. Fedchenko, J. Minár, A. Akashdeep, S. W. D'Souza, D. Vasilyev, O. Tkach, L. Odenbreit, Q. Nguyen, D. Kutnyakhov, N. Wind, L. Wenthaus, M. Scholz, K. Rossnagel, M. Hoesch, M. Aeschlimann, B. Stadtmüller, M. Kläui, G. Schönhense, T. Jungwirth, A. B. Hellenes, G. Jakob, L. Šmejkal, J. Sinova, and H.-J. Elmers, Observation of time-reversal symmetry breaking in the band structure of altermagnetic RuO_2, Science Advances **10**, eadj4883 (2024).

[12] Z. Lin, D. Chen, W. Lu, X. Liang, S. Feng, K. Yamagami, J. Osiecki, M. Leandersson, B. Thiagarajan, J. Liu, C. Felser, and J. Ma, Observation of giant spin splitting and d-wave spin texture in room temperature altermagnet RuO2 (2024), arXiv:2402.04995 [cond-mat.mtrl-sci].

[13] P. A. McClarty and J. G. Rau, Landau theory of altermagnetism, Phys. Rev. Lett. **132**, 176702 (2024).

[14] I. Turek, Altermagnetism and magnetic groups with pseudoscalar electron spin, Phys. Rev. B **106**, 094432 (2022).

[15] R. M. Sattigeri, G. Cuono, and C. Autieri, Altermagnetic surface states: towards the obser-

vation and utilization of altermagnetism in thin films, interfaces and topological materials, Nanoscale **15**, 16998 (2023).

[16] O. Gomonay, V. P. Kravchuk, R. Jaeschke-Ubiergo, K. V. Yershov, T. Jungwirth, L. Šmejkal, J. v. d. Brink, and J. Sinova, Structure, control, and dynamics of altermagnetic textures, npj Spintronics **2**, 35 (2024).

[17] R.-W. Zhang, C. Cui, R. Li, J. Duan, L. Li, Z.-M. Yu, and Y. Yao, Predictable gate-field control of spin in altermagnets with spin-layer coupling, Phys. Rev. Lett. **133**, 056401 (2024).

[18] I. Mazin, K. Koepernik, M. D. Johannes, R. González-Hernández, and L. Šmejkal, Prediction of unconventional magnetism in doped $FeSb_2$, Proceedings of the National Academy of Sciences **118**, e2108924118 (2021).

[19] I. Mazin (The PRX Editors), Editorial: Altermagnetism – a new punch line of fundamental magnetism, Phys. Rev. X **12**, 040002 (2022).

[20] H. Reichlova, R. Lopes Seeger, R. González-Hernández, I. Kounta, R. Schlitz, D. Kriegner, P. Ritzinger, M. Lammel, M. Leiviskä, A. Birk Hellenes, K. Olejník, V. Petřiček, P. Doležal, L. Horak, E. Schmoranzerova, A. Badura, S. Bertaina, A. Thomas, V. Baltz, L. Michez, J. Sinova, S. Goennenwein, T. Jungwirth, and L. Šmejkal, Observation of a spontaneous anomalous hall response in the Mn_5Si_3 d-wave altermagnet candidate, Nat. Commun. **15**, 4961 (2024).

[21] L. Šmejkal, R. González-Hernández, T. Jungwirth, and J. Sinova, Crystal time-reversal symmetry breaking and spontaneous Hall effect in collinear antiferromagnets, Science Advances **6**, eaaz8809 (2020).

[22] S. Zeng and Y.-J. Zhao, Description of two-dimensional altermagnetism: Categorization using spin group theory, Phys. Rev. B **110**, 054406 (2024).

[23] I. Mazin, R. González-Hernández, and L. Šmejkal, Induced monolayer altermagnetism in $MnP(S,Se)_3$ and FeSe (2023), arXiv:2309.02355 [cond-mat.mes-hall].

[24] R. B. Regmi, H. Bhandari, B. Thapa, Y. Hao, N. Sharma, J. McKenzie, X. Chen, A. Nayak, M. E. Gazzah, B. G. Márkus, L. Forró, X. Liu, H. Cao, J. F. Mitchell, I. I. Mazin, and N. J. Ghimire, Altermagnetism in the layered intercalated transition metal dichalcogenide $CoNb_4Se_8$ (2024), arXiv:2408.08835 [cond-mat.str-el].

[25] C. Autieri, G. Cuono, C. Noce, M. Rybak, K. Kotur, C. Agrapidis, K. Wohlfeld, and M. Birowska, Limited ferromagnetic interactions in monolayers of MPS_3 (M = Mn and Ni),

J. Phys. Chem. C **126**, 6791 (2022).

[26] R. Basnet, K. M. Kotur, M. Rybak, C. Stephenson, S. Bishop, C. Autieri, M. Birowska, and J. Hu, Controlling magnetic exchange and anisotropy by nonmagnetic ligand substitution in layered MPX_3 (M =Ni, Mn; X =S, Se), Phys. Rev. Res. **4**, 023256 (2022).

[27] W. M. Linhart, M. Rybak, M. Birowska, P. Scharoch, K. Mosina, V. Mazanek, D. Kaczorowski, Z. Sofer, and R. Kudrawiec, Optical markers of magnetic phase transition in CrSBr, J. Mater. Chem. C **11**, 8423 (2023).

[28] Z. Zhou, X. Cheng, M. Hu, J. Liu, F. Pan, and C. Song, Crystal design of altermagnetism (2024), arXiv:2403.07396 [cond-mat.mtrl-sci].

[29] B. Edwards, O. Dowinton, A. E. Hall, P. A. E. Murgatroyd, S. Buchberger, T. Antonelli, G. R. Siemann, A. Rajan, E. A. Morales, A. Zivanovic, C. Bigi, R. V. Belosludov, C. M. Polley, D. Carbone, D. A. Mayoh, G. Balakrishnan, M. S. Bahramy, and P. D. C. King, Giant valley-Zeeman coupling in the surface layer of an intercalated transition metal dichalcogenide, Nature Materials **22**, 459 (2023).

[30] N. Dale, O. A. Ashour, M. Vila, R. B. Regmi, J. Fox, C. W. Johnson, A. Fedorov, A. Stibor, N. J. Ghimire, and S. M. Griffin, Non-relativistic spin splitting above and below the Fermi level in a g-wave altermagnet (2024), arXiv:2411.18761 [cond-mat.mtrl-sci].

[31] M. Roig, A. Kreisel, Y. Yu, B. M. Andersen, and D. F. Agterberg, Minimal models for altermagnetism, Phys. Rev. B **110**, 144412 (2024).

[32] T. Mitsuhashi, M. Minohara, R. Yukawa, M. Kitamura, K. Horiba, M. Kobayashi, and H. Kumigashira, Influence of $k_\perp$ broadening on arpes spectra of the (110) and (001) surfaces of $\mathbf{srvo_3}$ films, Phys. Rev. B **94**, 125148 (2016).

[33] V. Popescu and A. Zunger, Extracting E versus $\vec{k}$ effective band structure from supercell calculations on alloys and impurities, Phys. Rev. B **85**, 085201 (2012).

[34] M. Weber, K. Leckron, L. Haag, R. Jaeschke-Ubiergo, L. Šmejkal, J. Sinova, and H. C. Schneider, Ultrafast electron dynamics in altermagnetic materials (2024), arXiv:2411.08160 [cond-mat.mtrl-sci].

[35] D. E. Moncton, J. D. Axe, and F. J. DiSalvo, Study of superlattice formation in $2H$-NbSe$_2$ and $2H$-TaSe$_2$ by neutron scattering, Phys. Rev. Lett. **34**, 734 (1975).

[36] F. Weber, S. Rosenkranz, J.-P. Castellan, R. Osborn, R. Hott, R. Heid, K.-P. Bohnen, T. Egami, A. H. Said, and D. Reznik, Extended phonon collapse and the origin of the charge-

density wave in $2H-\mathrm{NbSe}_2$, Phys. Rev. Lett. **107**, 107403 (2011).

[37] H. C. Mandujano, P. Y. Zavalij, A. Manjón-Sanz, H. Cao, and E. E. Rodriguez, Coexistence of commensurate and incommensurate antiferromagnetic groundstates in $\mathrm{Co}_x\mathrm{NbSe}_2$ single crystal (2024), arXiv:2501.00591 [cond-mat.mtrl-sci].

[38] P. Giannozzi, S. Baroni, N. Bonini, M. Calandra, R. Car, C. Cavazzoni, D. Ceresoli, G. L. Chiarotti, M. Cococcioni, I. Dabo, A. Dal Corso, S. de Gironcoli, S. Fabris, G. Fratesi, R. Gebauer, U. Gerstmann, C. Gougoussis, A. Kokalj, M. Lazzeri, L. Martin-Samos, N. Marzari, F. Mauri, R. Mazzarello, S. Paolini, A. Pasquarello, L. Paulatto, C. Sbraccia, S. Scandolo, G. Sclauzero, A. P. Seitsonen, A. Smogunov, P. Umari, and R. M. Wentzcovitch, QUANTUM ESPRESSO: a modular and open-source software project for quantum simulations of materials, Journal of Physics: Condensed Matter **21**, 395502 (19pp) (2009).

[39] P. Giannozzi, O. Andreussi, T. Brumme, O. Bunau, M. B. Nardelli, M. Calandra, R. Car, C. Cavazzoni, D. Ceresoli, M. Cococcioni, N. Colonna, I. Carnimeo, A. D. Corso, S. de Gironcoli, P. Delugas, R. A. D. Jr, A. Ferretti, A. Floris, G. Fratesi, G. Fugallo, R. Gebauer, U. Gerstmann, F. Giustino, T. Gorni, J. Jia, M. Kawamura, H.-Y. Ko, A. Kokalj, E. Küçükbenli, M. Lazzeri, M. Marsili, N. Marzari, F. Mauri, N. L. Nguyen, H.-V. Nguyen, A. O. de-la Roza, L. Paulatto, S. Poncé, D. Rocca, R. Sabatini, B. Santra, M. Schlipf, A. P. Seitsonen, A. Smogunov, I. Timrov, T. Thonhauser, P. Umari, N. Vast, X. Wu, and S. Baroni, Advanced capabilities for materials modelling with QUANTUM ESPRESSO, Journal of Physics: Condensed Matter **29**, 465901 (2017).

[40] J. P. Perdew, K. Burke, and M. Ernzerhof, Generalized gradient approximation made simple, Phys. Rev. Lett. **77**, 3865 (1996).

[41] M. Methfessel and A. T. Paxton, High-precision sampling for Brillouin-zone integration in metals, Phys. Rev. B **40**, 3616 (1989).

[42] D. Pacilè, C. Cardoso, G. Avvisati, I. Vobornik, C. Mariani, D. A. Leon, P. Bonfà, D. Varsano, A. Ferretti, and M. G. Betti, Narrowing of d bands of FeCo layers intercalated under graphene, Applied Physics Letters **118**, 121602 (2021).

Supplementary Information: Optical switching in a layered altermagnet

Alessandro De Vita***,[1,2] Chiara Bigi***,[3,*] Davide Romanin***,[4] Matthew D. Watson,[5] Vincent Polewczyk,[6] Marta Zonno,[3] François Bertran,[3] My Bang Petersen,[7] Federico Motti,[8] Giovanni Vinai,[8] Manuel Tuniz,[9] Federico Cilento,[10] Mario Cuoco,[11] Brian M. Andersen,[12] Andreas Kreisel,[12] Luciano Jacopo D'Onofrio,[11] Oliver J. Clark,[13] Mark T. Edmonds,[13] Christopher Candelora,[14] Muxian Xu,[14] Siyu Cheng,[14] Alexander LaFleur,[14] Tommaso Antonelli,[15] Giorgio Sangiovanni,[16] Lorenzo Del Re,[16] Ivana Vobornik,[8] Jun Fujii,[8] Fabio Miletto Granozio,[17] Alessia Sambri,[17] Emiliano Di Gennaro,[18] Jeppe B. Jacobsen,[19] Henrik Jacobsen,[20] Ralph Ernstorfer,[1,2] Ilija Zeljkovic,[14,†] Younghun Hwang,[21,‡] Matteo Calandra,[22,§] Jill A. Miwa,[7,¶] and Federico Mazzola[17,**]

[1]*Institut für Optik und Atomare Physik, Technische Universität Berlin,*
Straße des 17 Juni 135, 10623 Berlin, Germany
[2]*Fritz Haber Institut der Max Planck Gesellshaft,*
Faradayweg 4–6, 14195 Berlin, Germany
[3]*Synchrotron SOLEIL, F-91190 Saint-Aubin, France*
[4]*Université Paris-Saclay, CNRS, Centre de Nanosciences*
et de Nanotechnologies, 91120, Palaiseau, Paris, France.
[5]*Diamond Light Source, Harwell Campus,*
Didcot, OX11 0DE, United Kingdom
[6]*Université Paris-Saclay, UVSQ, CNRS, GEMaC, 78000, Versailles, France*
[7]*Department of Physics and Astronomy,*
Interdisciplinary Nanoscience Center,
Aarhus University, 8000 Aarhus C, Denmark
[8]*CNR - Istituto Officina dei Materiali (IOM), I-34139 Trieste, Italy*
[9]*Dipartimento di Fisica, Universita degli studi di Trieste, 34127, Trieste, Italy*
[10]*Elettra - Sincrotrone Trieste S.C.p.A.,*
Strada Statale 14, km 163.5, Trieste, Italy
[11]*CNR-SPIN, c/o Universitá di Salerno, IT-84084 Fisciano (SA), Italy*
[12]*Niels Bohr Institute, University of Copenhagen, 2100 Copenhagen, Denmark*

[13]*School of Physics and Astronomy,*
Monash University, Clayton, Victoria 3800, Australia
[14]*Department of Physics, Boston College, Chestnut Hill, MA 02467, USA*
[15]*ETH Zürich, HPF E 19 Otto-Stern-Weg 1, 8093 Zürich, Switzerland*
[16]*Institute for Theoretical Physics and Astrophysics,*
University of Würzburg, D-97074 Würzburg, Germany
[17]*CNR-SPIN, c/o Complesso di Monte S. Angelo, IT-80126 Napoli, Italy*
[18]*Physics Department, University of Napoli "Federico II",*
Via Cinthia, 21, Napoli 80126, Italy
[19]*Nanoscience Center, Niels Bohr Institute,*
University of Copenhagen, 2100 Copenhagen, Denmark
[20]*European Spallation Source ERIC - Data Management*
and Software Center, 2800 Kgs. Lyngby, Denmark
[21]*Electricity and Electronics and Semiconductor Applications,*
Ulsan College, Ulsan 44610, Republic of Korea
[22]*Department of Physics, University of Trento,*
Via Sommarive 14, Povo 38123, Italy

*** These authors contributed equally.

High-purity single crystals, synthesized as detailed in the Methods Section, underwent comprehensive characterization by X-ray diffraction (XRD), low-energy electron diffraction (LEED), resistivity measurements, X-ray photoelectron spectroscopy (XPS), pump-probe optical spectroscopy, and scanning tunnelling microscopy (STM). These complementary analyses established the structural and electronic behaviour of the samples, underpinning investigations using high-resolution angle-resolved photoelectron spectroscopy (ARPES), ARPES with few-micron spatial resolution resolution (microARPES) and spin-resolved ARPES (spinARPES). In this section, we present an in-depth detailed discussion of the characterization outcomes, alongside additional ARPES-type data that support the findings of the main text.

---

[*] chiara.bigi@synchrotron-soleil.fr
[†] ilija.zeljkovic@bc.edu
[‡] younghh@uc.ac.kr
[§] m.calandrabuonaura@unitn.it
[¶] miwa@phys.au.dk
[**] federico.mazzola@spin.cnr.it

I. Structural characterization of $Co_{1/4}NbSe_2$

In this section, we present structural characterization and basic transport measurements of $Co_{1/4}NbSe_2$. XRD measurements confirm a clean and well-ordered crystalline structure consistent with the $NbSe_2$ lattice. Using data acquired with a D8 Advance Bruker diffractometer, we applied Bragg's law to analyze the positions of the intense diffraction peaks – 002, 004, 006, and 008 – shown in Fig. S1a. From this analysis, we extracted an out-of-plane (c-axis) lattice parameter of 12.59 Å. This value closely matches the reported c-axis lattice parameter of 12.55 Å, indicating that the incorporation of a small amount of Co slightly enlarges the interlayer spacing in bulk transition metal dichalcogenides like $NbSe_2$.

An illustration of the $Co_{1/4}NbSe_2$ crystal structure is provided in Fig. S1b. The $NbSe_2$ unit is depicted as a purple triangular prism, while the Co atoms are shown as yellow spheres. The Co atoms double the unit cell, giving a 2×2 modulation. Such atoms are positioned between the single $NbSe_2$ layers, with the c-axis lattice parameter determined by the XRD measurements. The magnetic moments of the Co atoms are represented by red and blue arrows in the schematic and give rise to an alternating up-down stacking along the c-axis, which yields an overall zero magnetic moment.

In addition, resistivity measurements were performed, as shown in Fig. S1c. The resistivity decreases smoothly from room temperature to 50 K, at which point a rapid drop is observed. This behavior could suggest the presence of a magnetic phase transition and we attribute it to the Curie temperature (T_C).

Finally, LEED measurements were performed at $E_k = 145\,\text{eV}$ with the sample held at 15 K, well below T_C observed in the transport measurements. The LEED image, shown in Fig. S1d, reveals sharp first-order spots associated with $NbSe_2$ units, which are clearly arranged in a hexagonal pattern and denoted by blue circles. Additionally, dimmer but noticeable spots form a 2×2 pattern, highlighted by orange circles, corresponding to the Co atoms. These observations corroborate the crystal structure depicted in Fig. S1b and provide further evidence for the structural order of the sample at low temperatures. The sharpness of the observed spots point to high quality crystalline $Co_{1/4}NbSe_2$, in agreement with the XRD data.

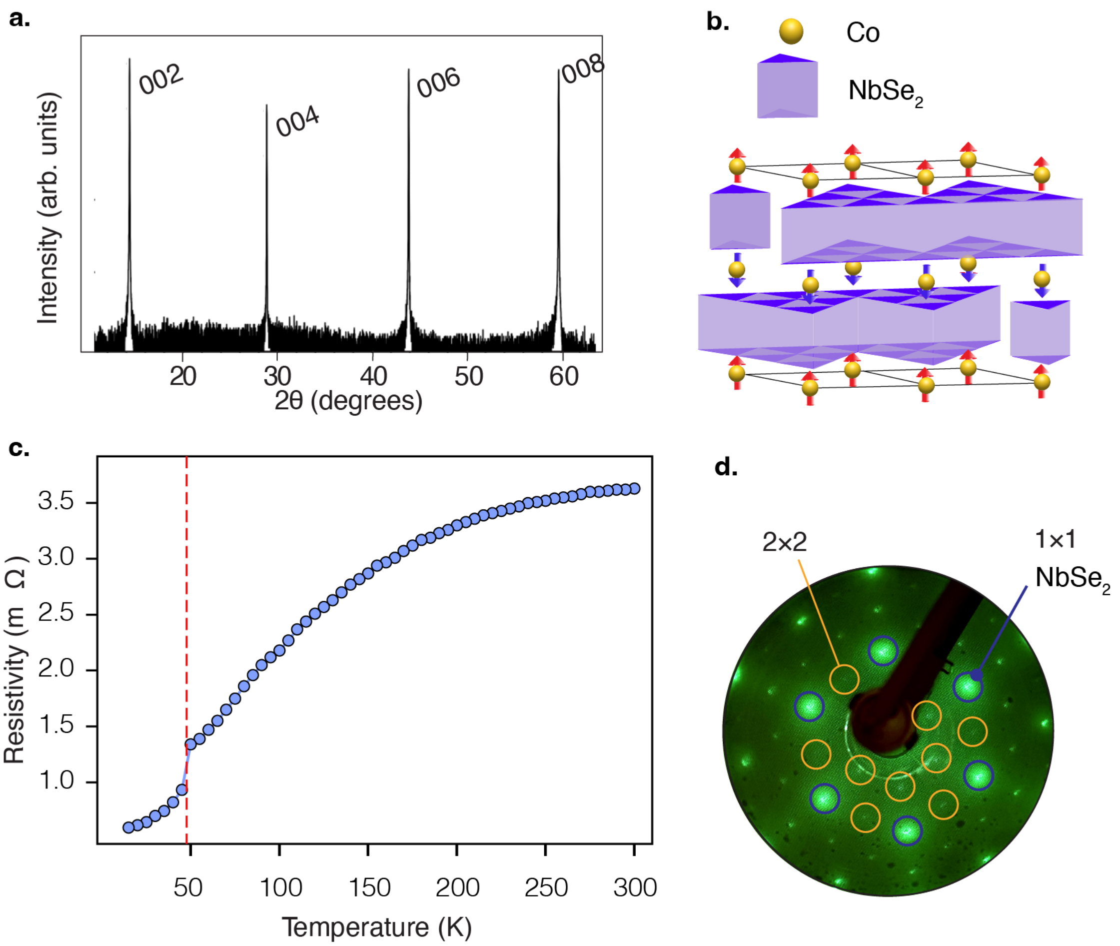

FIG. S1. **Crystal structure properties of Co$_{1/4}$NbSe$_2$.** **a.** XRD measurements of the Co$_{1/4}$NbSe$_2$ reveal a c-axis lattice parameter of 12.59 Å. **b.** A three-dimensional illustration of the real-space crystal structure of Co$_{1/4}$NbSe$_2$, with yellow spheres representing Co atoms and a purple triangular prism corresponding to a single NbSe$_2$ unit. Red and blue arrows overlaid on the Co atoms indicate their magnetic moments. **c.** Resistivity measurements as a function of temperature, with a notable drop in resistivity at 50 K marked by a vertical dashed red line. **d.** LEED data acquired at 145 eV showing the reconstruction: the orange circles indicate the 2×2 features, while the blue circles mark the primitive 1×1 ones.

II. STM data pertaining to the formation of the Co surface termination and step height of Co$_{1/4}$NbSe$_2$.

In this section, we present additional STM data for the Co$_{1/4}$NbSe$_2$ sample. In Fig. S2a, a topographic image of the Co surface termination is shown. This image was acquired

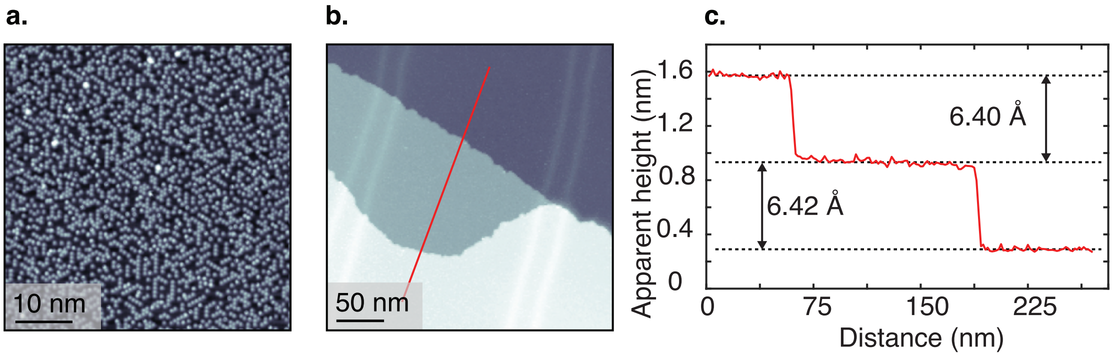

FIG. S2. **STM images of the cobalt surface termination and step height analysis. a.** STM topographic image of the Co surface termination acquired within 500 nm of the area shown in Fig. 1f in the main text. **b.** A large area STM topographic image showing two Se step-edges. The overlaid red line indicates where the line profile in panel c. was acquired. **c.** The line profile showing an apparent step height of ≈ 6.40 Å, which matches closely with the ≈ 6.7 Å separation between Se layers within a pristine 2H-NbSe$_2$ unit cell. [Ref.] All images presented here were acquired scanning parameters: $V_{sample} = 500\,\mathrm{mV}$ and $I_{set} = 10\,\mathrm{pA}$

.

approximately 500 nm away from the Co surface termination imaged in Fig. 1f of the main text. The two images exhibit noticeable differences: the STM image in the main text displays a well-ordered hexagonal arrangement of atoms which give rise to a 2×2 modulation, whereas the image here reveals an excess of small bright protrusions with some degree of local ordering. An FFT of this STM topograph (not shown) indicates a faint 2×2 modulation. While this region does not exhibit a fully developed 2×2 modulation, the Co atoms appear to partially form the structure. We note that these samples were cleaved under ultra-high vacuum conditions at approximately few tens of K. Consequently, it is not surprising that the Co termination exhibits differing degrees of Co ordering.

In Fig. S2b, a larger area of the sample is shown, displaying three distinct terraces. A line profile extracted along the red line in Fig. S2c reveals the apparent step height of the terraces. The measured step height of 6.40 Å closely matches the approximate 6.7 Å separation between Se layers in pristine 2H-NbSe$_2$ bulk crystal. This smaller value is consistent with the reduced c-axis lattice parameter measured by XRD, which indicates a step height of 6.30 Å; see Section I.

III. Chemical characterization of Co$_{1/4}$NbSe$_2$

The chemical composition of the sample was qualitatively and quantitatively analyzed using synchrotron-based XPS in the soft X-ray regime (APE-HE beamline at the Elettra synchrotron radiation facility in Trieste, Italy). The measurement geometry is illustrated in Fig. S3a. Linearly polarized X-rays with an energy of 1200 eV (red arrow) were incident on the sample surface at an angle of 45°, with the polarization direction indicated by the blue arrow. A photoemitted electron is represented by the green circle and arrow. An overview XPS spectrum of the sample is shown in Fig. S3b, where the major peaks are identified and correspond to the expected elemental composition of the sample. This result confirms that the sample is free of contaminants, demonstrating that cleaving under ultrahigh vacuum conditions at low temperatures is an effective method for sample preparation.

As shown in Fig. S3c–d, high-resolution spectra were acquired around the Co $2p$, Nb $3d$, and Se $3d$ peaks to determine the stoichiometry of the sample, confirming that it matches the expected composition. The dashed blue line beneath the data in each panel represents the subtracted Shirley background. The as-measured peak intensities are shown on the left axis in blue, while the integrated values are displayed on the right axis in red. The Co $2p$ peaks are located at 402 eV and 417 eV kinetic energy, with an expected separation of 15 eV. The Nb $3d$ spectrum exhibits a relatively larger cross-section than Co $2p$, with two well-defined peaks at 988.5 eV and 991 eV and a separation of 2.5 eV. The Se $3d$ spectrum, also characterized by a large cross-section, displays a single dominant peak at 1140 eV. Together, the Nb $3d$ and Se $3d$ core-level spectra indicate a NbSe$_2$ chemical composition. Comparison with the Co $2p$ spectrum reveals a stoichiometry of Co$_{1/4}$NbSe$_2$, with one Co atom for every four Nb atoms.

IV. Time-resolved reflectivity measurements of Co$_{1/4}$NbSe$_2$

We performed time-resolved reflectivity measurements on the Co$_{1/4}$NbSe$_2$ sample at the T-Rex Laboratory of the FERMI free-electron laser (FEL) at Elettra. Figure S4 presents two-dimensional (2D) maps of the $\Delta R/R$ signal as a function of both probe wavelength and delay time for three sample temperatures: 300 K, 80 K, and 20 K. In these maps, red indicates a positive $\Delta R/R$ value, while blue represents a negative $\Delta R/R$ value. At 300 K,

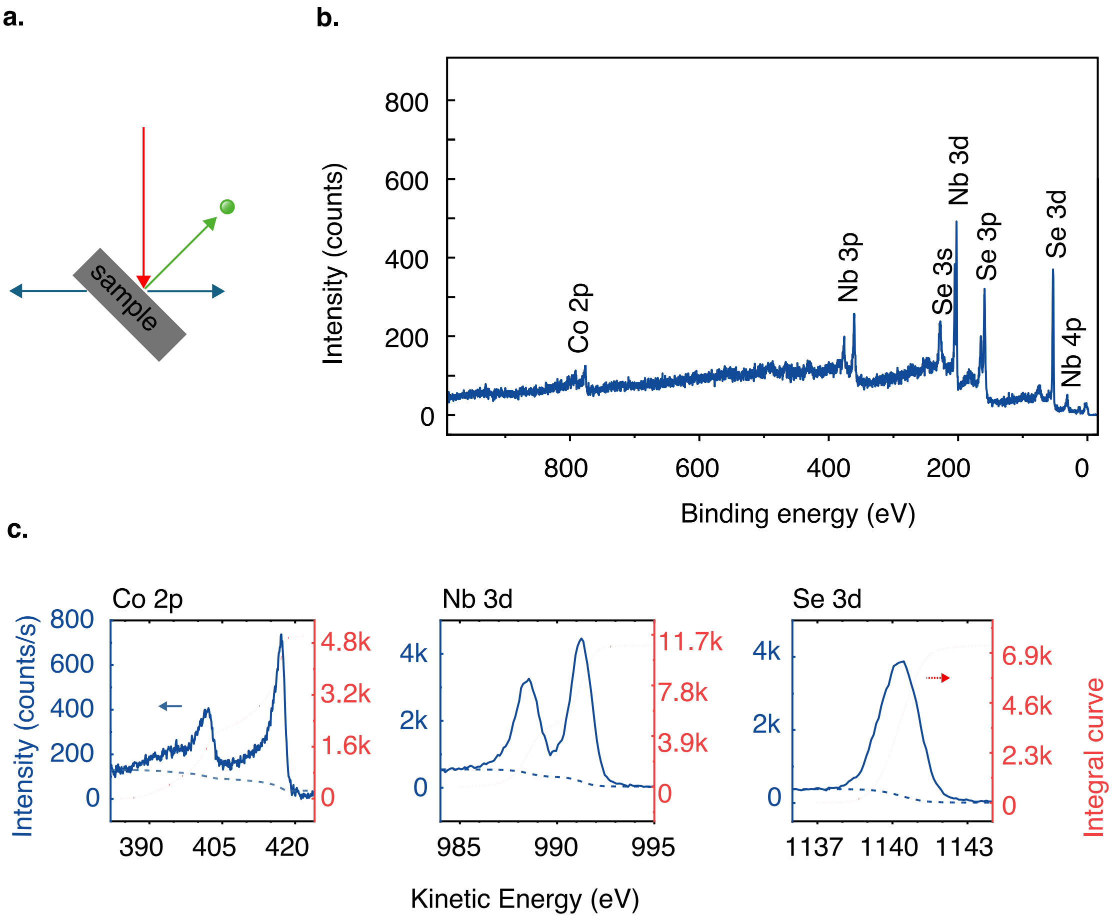

FIG. S3. **XPS measurements to identify elemental contributions.** **a.** Schematic of the measurement setup, illustrating the X-ray (red arrow) and sample (gray block) geometry, the direction of the incoming electric field (double-headed blue arrow), and the emission of a photoemitted electron (green arrow and sphere). X-rays with a photon energy of 1200 eV were linearly polarized in the horizontal plane and incident on the sample surface at 45°. **b.** Overview XPS scan displaying intensity as a function of binding energy. Dominant peaks are labeled and correspond to the expected peaks for $Co_{1/4}NbSe_2$. The data confirms that cleaving under ultra-high vacuum conditions ($\approx 1 \times 10^{-10}$ mbar) at low temperature (70 K) produces clean surfaces with no detectable contamination. **c.–e.** Core-level spectra for Co $2p$, Nb $3d$ and Se $3d$ used to quantify the stoichiometry of the sample. The dashed blue line beneath the peaks represents the subtracted Shirley background. The core levels were integrated, with the red scale shown on the right of each panel and the as-measured intensity displayed on the left blue axes.

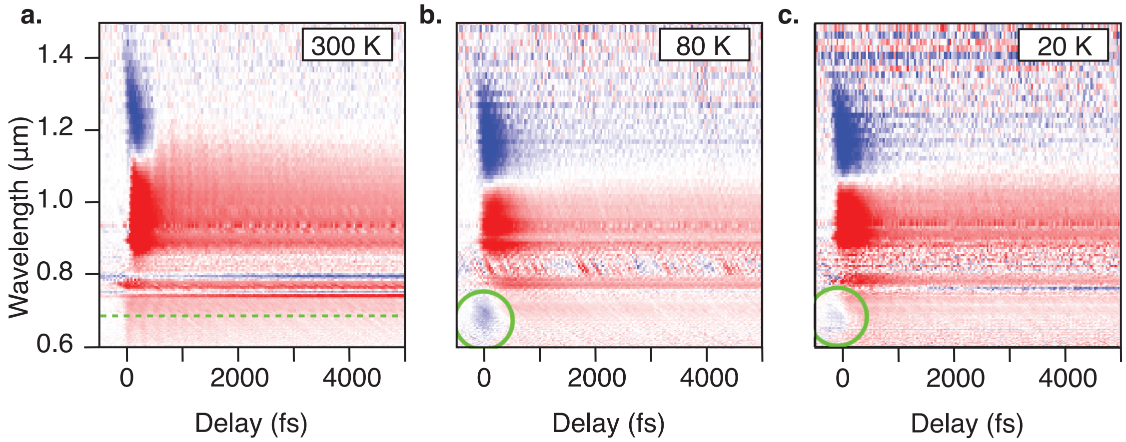

FIG. S4. **Time-resolved reflectivity measurements of $\mathrm{Co}_{1/4}\mathrm{NbSe}_2$ for different sample temperatures. a.** The ΔR/R signal is shown as a function of probe wavelength (vertical axis) and delay time (horizontal axis for the sample held at 300 K. The pump power is 30 mW. The red colour corresponds to $\Delta R/R > 0$ and the blue colour to $\Delta R/R < 0$. **b.** The same time-resolved reflectivity measurements are shown for a sample temperature of 80 K. Note that at time zero, there is a change in the sign of the $\Delta R/R$ signal value below 0.8 µm wavelength, as denoted by the green circle. **c.** Here, the sample temperature is 20 K. Notably the $\Delta R/R$ signal value at larger wavelengths are less impacted by sample temperature, whereas the absolute value of the $\Delta R/R$ signal within the green circle is diminished.

with 500 µJ cm^{-2} pump fluence, we detect coherent oscillations in the visible range, signaling the excitation of a coherent phonon with a frequency of approximately 4 THz (Fig. S4a). At 80 K, we observe a change in the $\Delta R/R$ signal from positive to negative near time zero at shorter wavelengths, as highlighted by the green circle in Fig. S4b. This temperature-dependent sign reversal is pronounced when compared to the 300 K data in Fig. S4a. At 20 K, a similar change in sign is observed, albeit to a lesser extent (Fig. S4c). Notably, $\Delta R/R$ at longer wavelengths, specifically greater than 700 nm, remains largely unaffected by changes in sample temperature.

In Fig. S5, the time profile extracted at $\lambda = 700$ nm from the data in Fig. S4a is shown. Coherent oscillations are clearly visible in Fig. S5a. By isolating the oscillatory component and performing a fast Fourier transform (FFT), we obtain the frequency spectrum of the excited phonon mode (Fig. S5b). The peak in the spectrum is located at approximately 4 THz, identifying the frequency of the phonon.

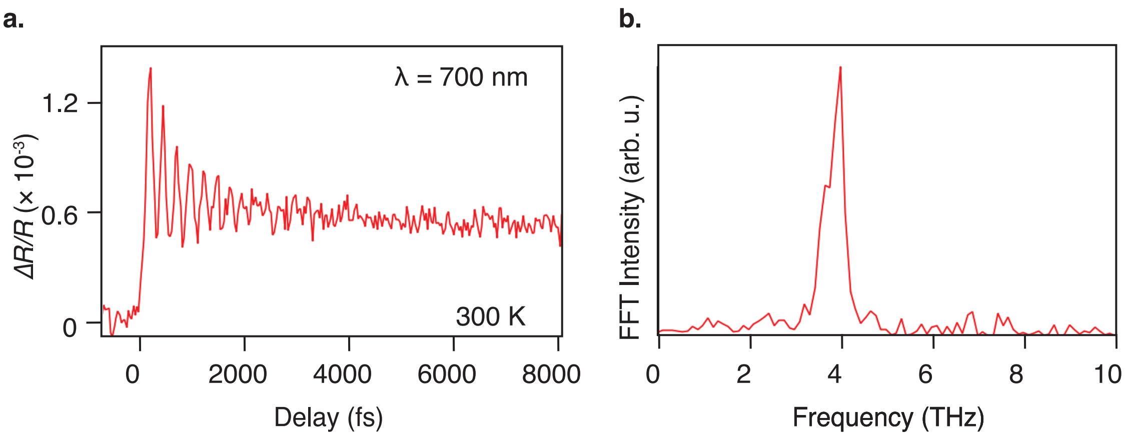

FIG. S5. **Identifying the phonon frequency.** **a.** The time profile (red) extracted at $\lambda = 700\,\mathrm{nm}$ from the data in Fig. S4a. **b.** The FFT of the time profile showing a clear peak at approximately 4 THz. This is the phonon frequency.

To investigate the spectral feature that exhibits a strong temperature dependence – specifically the feature highlighted by the green circle in Fig. S4b and c – we performed time-resolved reflectivity experiments using a single-color probe at $\lambda = 650\,\mathrm{nm}$. The results of a temperature scan are shown in Fig. S6. This scan reveals that the spectral feature, characterized by a negative $\Delta R/R$ signal near time zero, disappears above $T \approx 130\,\mathrm{K}$, as discussed in the main text.

V. Additional ARPES measurements of $Co_{1/4}NbSe_2$.

The data acquired using different ARPES techniques are colour-coded for clarity. ARPES data with few-micrometer-sized spatial resolution (microARPES) are presented in a "bone" color scheme, high-energy resolution ARPES data in "purple/white," and spin-ARPES data in "red/blue." The low temperature microARPES measurements were conducted at the I05 beamline at the Diamond Light Source in Didcot, United Kingdom, and the room temperature data at the SGM4 beamline at ASTRID2 in Aarhus, Denmark [1, 2]. High-resolution ARPES data were collected at the CASSIOPEE beamline at Soleil Synchrotron in France, while spinARPES data were obtained at the LE-APE beamline at the Elettra Synchrotron in Trieste, Italy.

In this section, we provide additional ARPES data acquired at additional photon energies

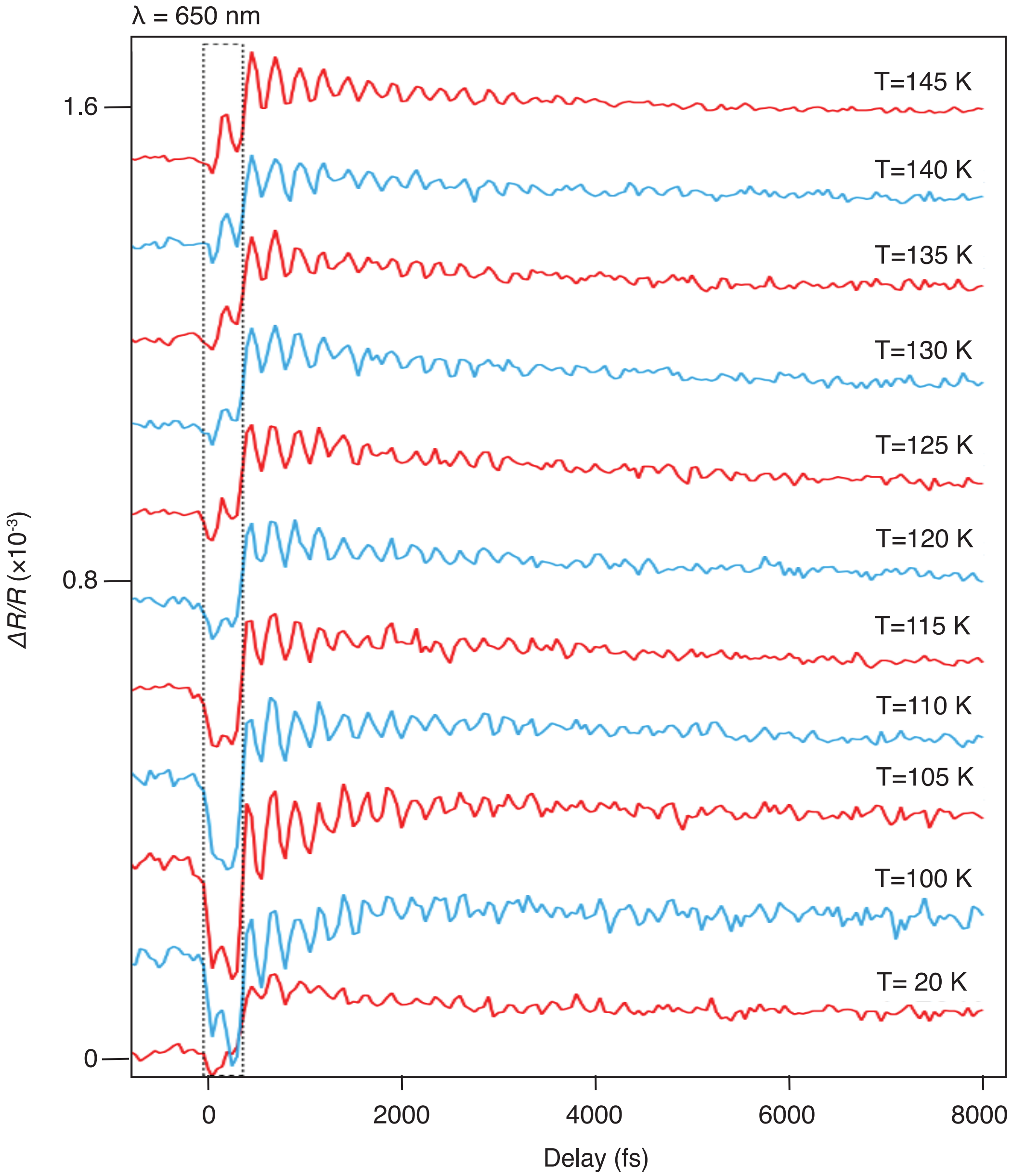

FIG. S6. **A temperature dependent spectral feature. a.** Time-resolved reflectivity experiment using a single 650 nm probe as a function of temperature, with the sample heated from 20 K to 145 K. The time profiles are displayed in alternating red and blue colours to distinguish sequential temperatures. Black dotted lines demarcate the spectral feature of interest near time zero. The negative $\Delta R/R$ spectral feature persists from 20 K to 140 K, disappearing at higher temperatures. The temperature scan was conducted at a pump power of 18 mW.

for low, intermediate and high temperatures to supplement the ARPES data in the main text.

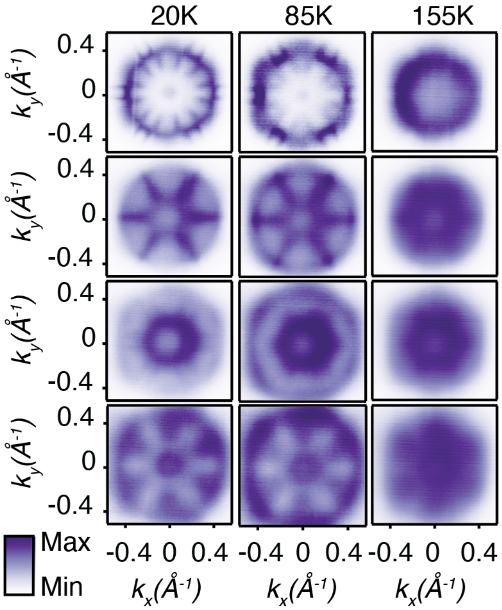

FIG. S7. **$Co_{1/4}NbSe_2$ constant energy maps at different sample temperatures.** Constant energy maps obtained using photons with an energy of 25 eV are shown for $E - E_F = 0\,eV$, $E - E_F = 0.1\,eV$, $E - E_F = 0.2\,eV$, and $E - E_F = 0.3\,eV$ at three different sample temperatures: 20 K, 85 K, and 155 K.

In Fig. S7, we compare constant energy maps acquired using 25 eV at three different temperatures: 20 K, 85 K, and 155 K. For each photon energy and temperature, constant energy maps are presented at $E - E_F = 0\,eV$, $E - E_F = 0.1\,eV$, $E - E_F = 0.2\,eV$, and $E - E_F = 0.3\,eV$. At first glance, the Fermi surface resembles that of bulk 2H-$NbSe_2$, with a large hexagonal pocket at the zone center, as evident in the constant energy maps acquired with 70 eV photons. However, notable differences are evident, where back-folding of the bands is observed, consistent with a 2×2 reconstruction. As the sample temperature increases from 20 K to 155 K, the back-folding of the bands disappears, accompanied by an overall thermal broadening of the bands.

Additionally, in Fig. S8, we present microARPES measurements acquired from the same sample position at different photon energies (37.5 eV, 44 eV, 47.5 eV, and 55 eV) and light polarizations (LH and LV) at two distinct temperatures, 24 K and 70 K. The data reveal significant changes in the overall spectral bandwidth with temperature. Notably, these

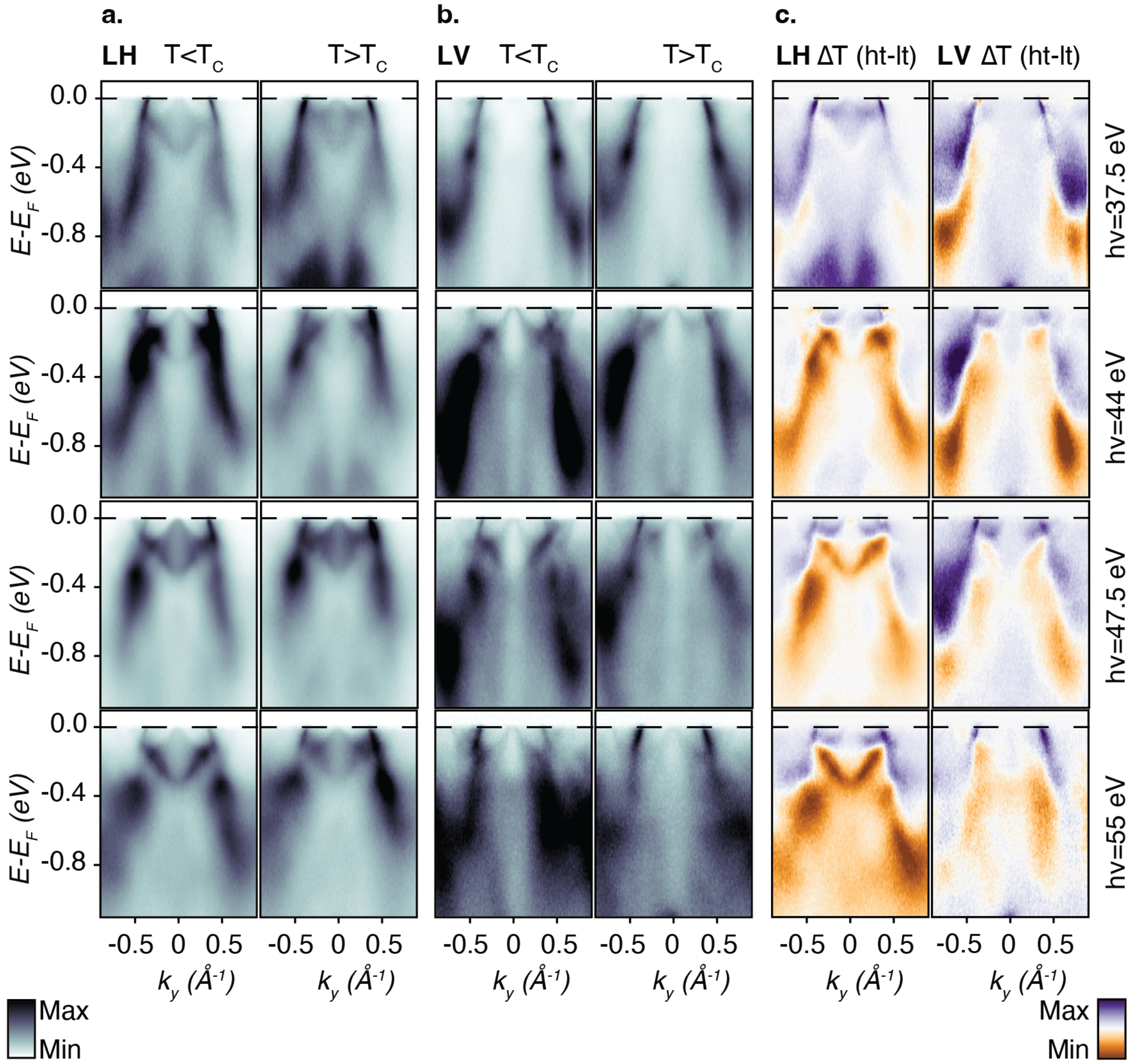

FIG. S8. **MicroARPES measurements of $Co_{1/4}NbSe_2$ were acquired above and below T_C.** **a.** Comparison of the electronic structure across the transition temperature, with data collected below T_C (left column) and above T_C (right column) along the Γ–M direction for three photon energies, as indicated on the right-hand side. The spectra were recorded using LH polarization. **b.** Corresponding measurements obtained with LV polarization. **c.** Difference spectra highlighting changes between the high- and low-temperature electronic structures, acquired from the same spot on the sample using both polarizations. The data reveal pronounced temperature-dependent modifications, consistent with a reduction in spectral bandwidth above the critical temperature.

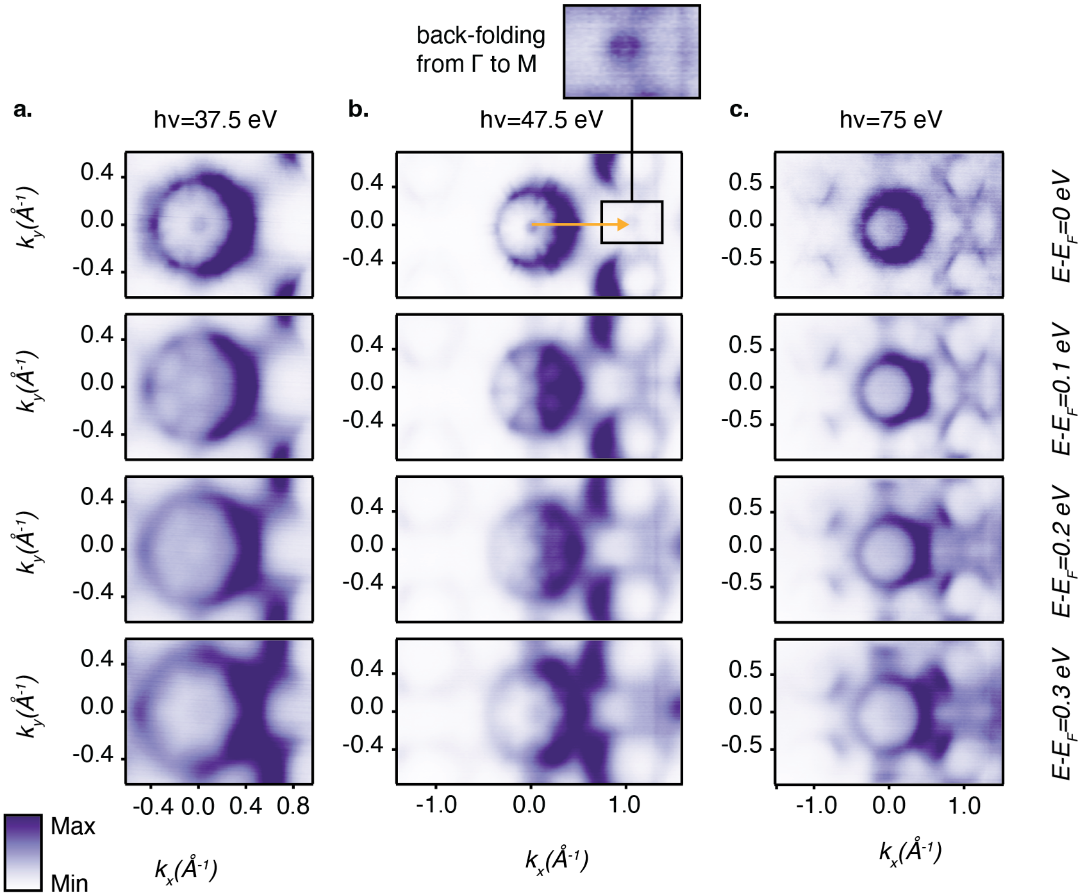

FIG. S9. **Comparison of $Co_{1/4}NbSe_2$ constant energy maps acquired at different photon energies. a.** Constant energy maps obtained using photons with an energy of 37.5 eV are shown for $E - E_F = 0.1$ eV, $E - E_F = 0.1$ eV, $E - E_F = 0.2$ eV, and $E - E_F = 0.3$ eV. This photon energy corresponds to the A-point in the 3D BZ. **b.** Corresponding measurements acquired using a photon energy of 47.5 eV and **c.** 75 eV. The inset shows the back-folding of the bands from Γ to M. Notably, 47.5 eV corresponds to the Γ-point in the 3D BZ.

changes cannot be explained by a simple rigid shift model, as many spectral features remain fixed in energy and momentum. Instead, the observed temperature-dependent modifications are likely linked to large-scale effects of magnetic ordering. Despite the broader spectral features at higher temperatures, the energy splitting remains discernible, suggesting the persistence of local magnetic moments within the thermal energy range explored.

In Fig. S9, we present constant energy maps of $Co_{1/4}NbSe_2$ at $E - E_F = 0$ eV, $E - E_F = 0.1$ eV, $E - E_F = 0.2$ eV, and $E - E_F = 0.3$ eV for three photon energies: 37.5 eV, 47.5 eV, and 75 eV. At the Fermi level, the fermiology predominantly exhibits a two-dimensional

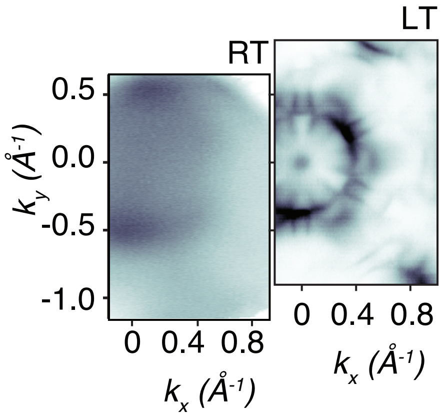

FIG. S10. **Comparison of $Co_{1/4}NbSe_2$ constant energy maps acquired at different sample temperature.** Fermi surface ($E - E_F = 0$) acquired with the sample fixed at 300 K (left) and 25 K (right) at a photon energy of 45. eV and LV polarization.

character. Varying the photon energy effectively tunes the matrix elements, enhancing the visibility of distinct spectral features.

In Fig. S10, we compare constant-energy maps of $Co_{1/4}NbSe_2$ at $E - E_F = 0$ acquired using microARPES at 300 K (left panel) and 25 K (right panel). At 300 K, the bands are considerably broader than at 25 K, obscuring many finer details—particularly the 2×2 ordering. A more detailed microARPES analysis, conducted at 25 K with additional photon energies and spanning multiple high-symmetry points along k_z, is shown in Fig. S11.

For completeness, we also present energy versus momentum spectra acquired along the Γ–M and Γ–K high-symmetry directions in Fig. S12 and Fig. S13, respectively. The primary observation is a redistribution of spectral weight across the bands, indicating the presence of complex matrix elements and necessitating that the electronic structure of $Co_{1/4}NbSe_2$ be investigated using multiple photon energies. Notably, the large c-axis parameter contributes to significant k_z broadening. This implies that even with a single photon energy, a substantial portion of the Brillouin zone is probed, effectively manifesting as an apparent two-dimensionality of the bands, despite their potential bulk character.

Again, for completeness, we present the calculated electronic structure with the corresponding spectral weight and spin channels along the Γ–K direction in Fig. S14, supplementing the calculated electronic structure along the Γ–M direction shown in the main text. The agreement with the experimental results is excellent, further corroborating the findings

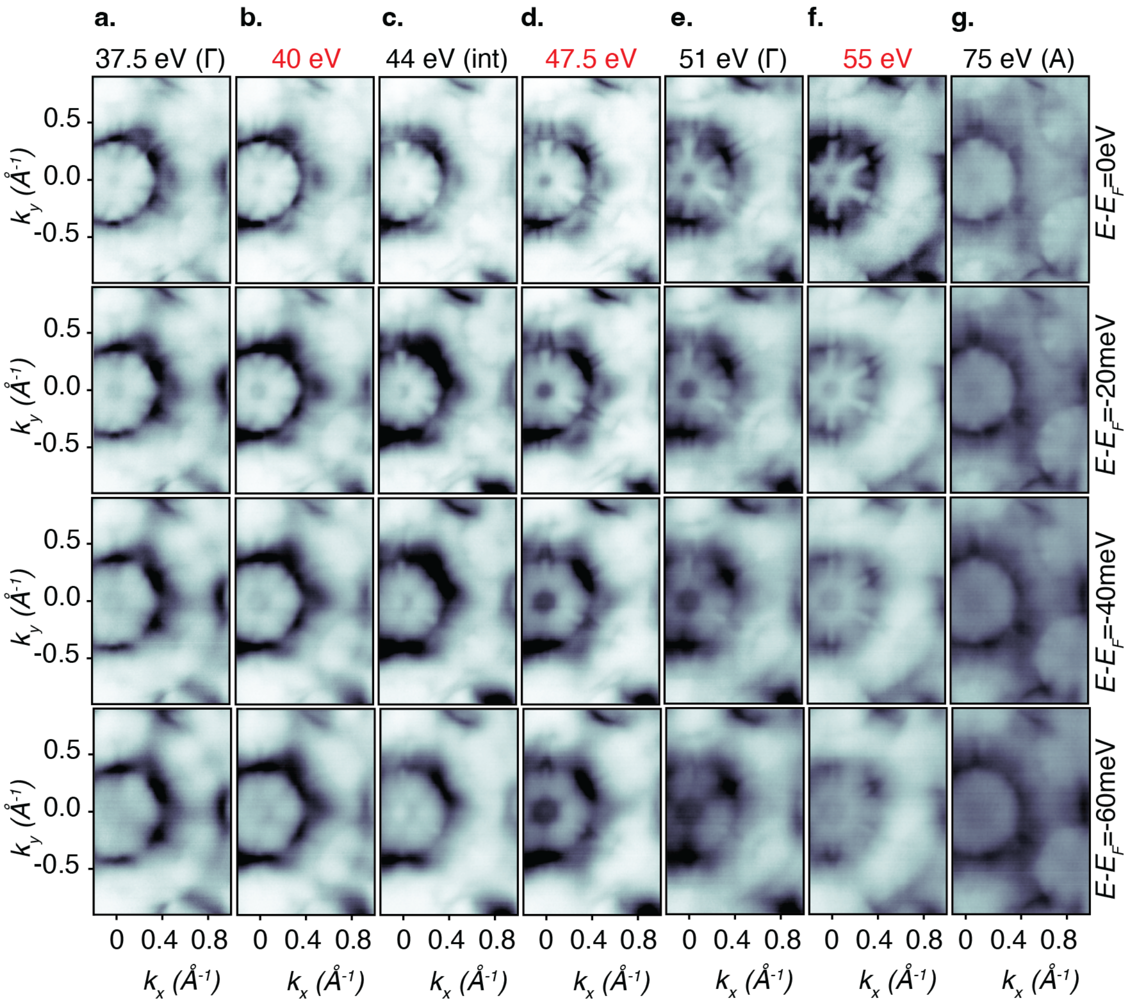

FIG. S11. **$\mathrm{Co}_{1/4}\mathrm{NbSe}_2$ constant energy maps acquired with microARPES.** From **a** to **g** multiple photon energies have been used ranging across multiple BZs in k_z. The bulk high symmetry points have been clearly stated, with red colour (or "int") indicating a k_z in between the A-point and Γ-point. (Note that the red colour should be approximately a distance of 0.25 Å^{-1} in k_z from the A-point towards the Γ-point.) Each column indicates a different binding energy to help visualize the electronic structure below the Fermi level.

of our study.

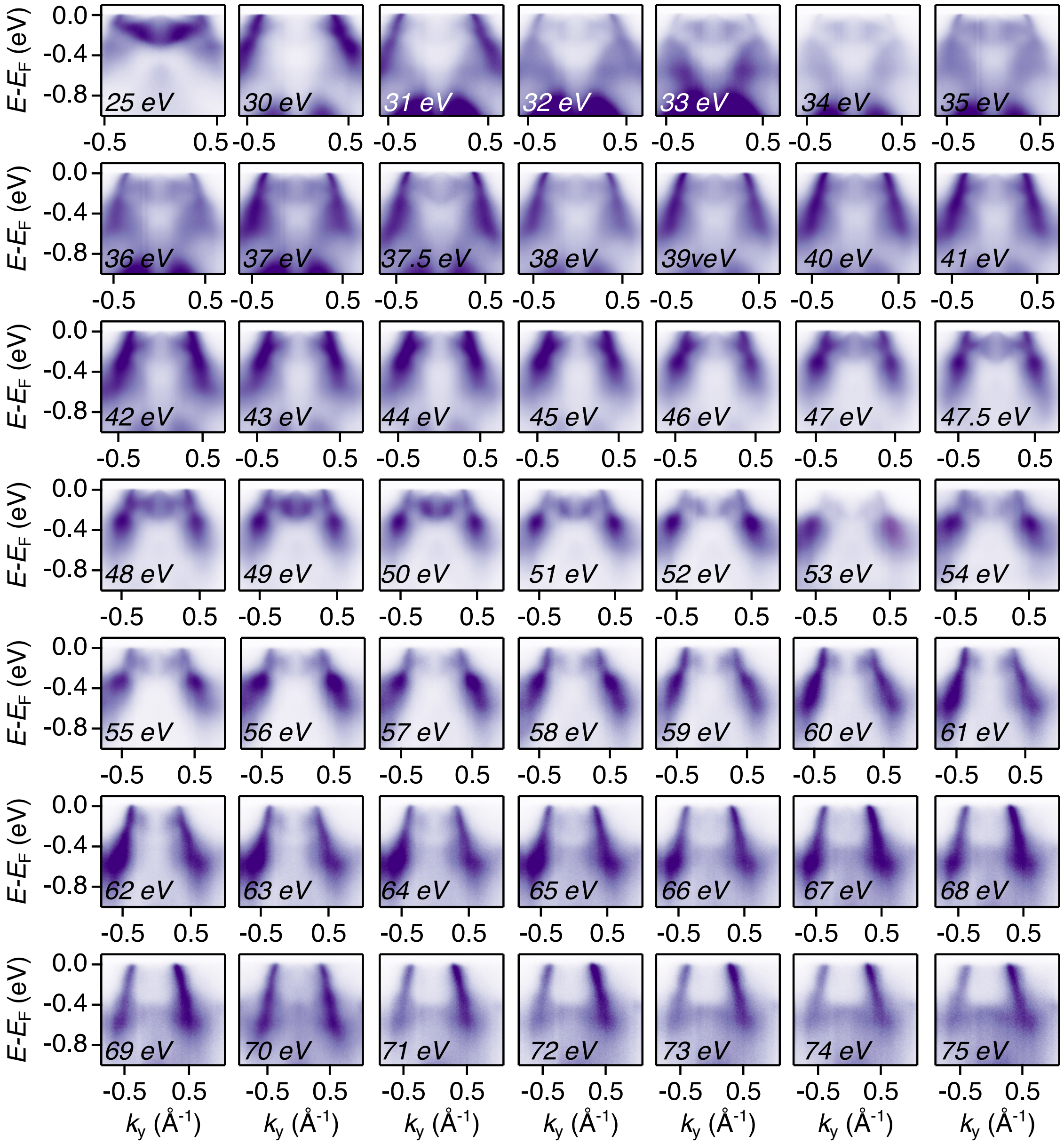

FIG. S12. **$Co_{1/4}NbSe_2$ energy versus momentum spectra along Γ-M.** The electronic structure measured by using LH light polarization is shown as function of photon energy.

VI. Ab-initio energetics of $Co_{1/4}NbSe_2$.

In order to determine the most energetically favored position for the Co atoms in the 2×2 $NbSe_2$ supercell, we have fully relaxed the 4 possible configurations (Fig. S15) and computed the total energy per Nb atom. Results are summarized in Tab. S1. We can observe that the most stable Co intercalations are such that the Co atom is directly above and below two Nb atoms.

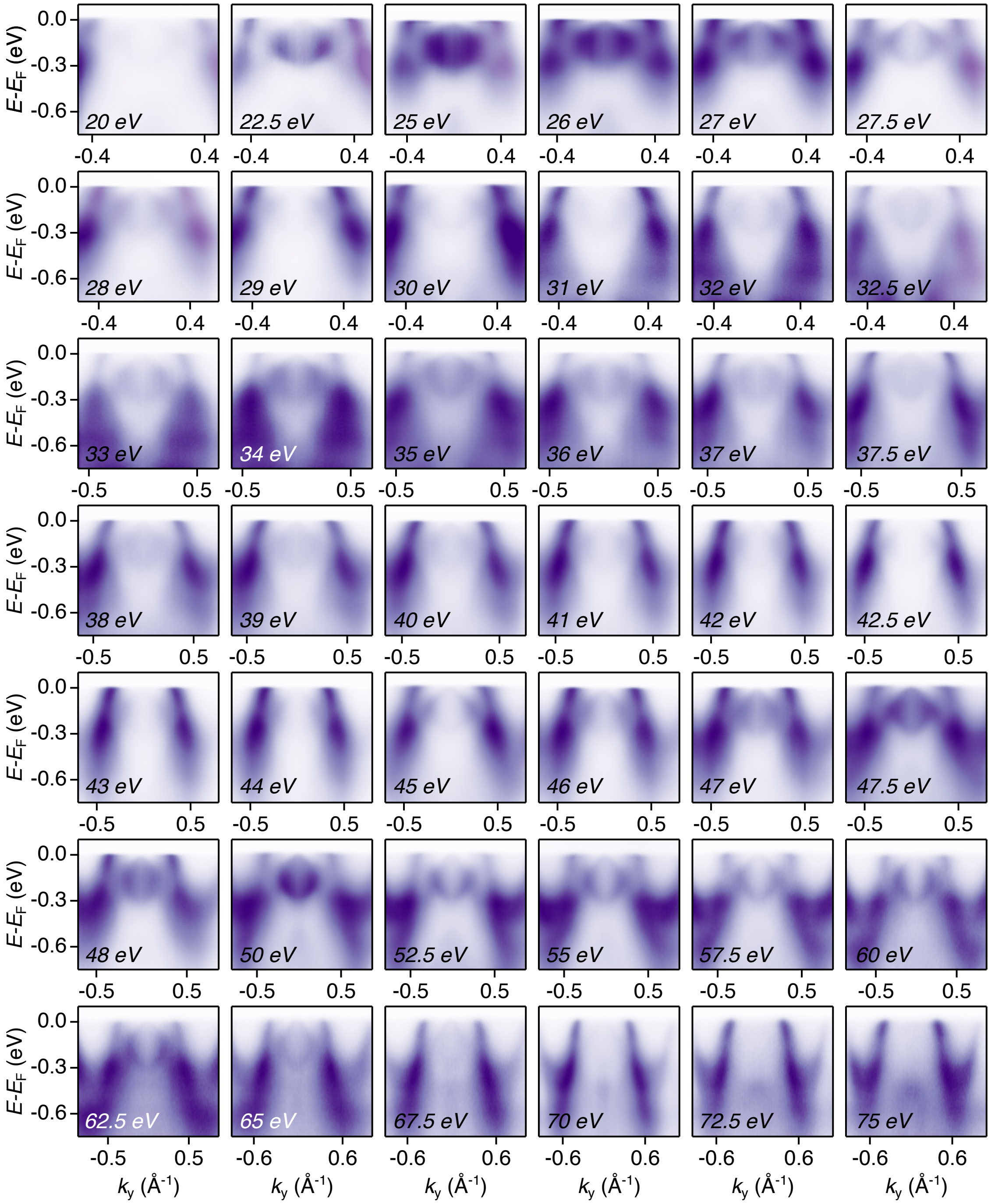

FIG. S13. **Co$_{1/4}$NbSe$_2$ energy versus momentum spectra along Γ-K.** The electronic structure measured by using LH light polarization is shown as function of photon energy.

After that, we proceeded to further relax the most stable configurations (03 and 04, Fig. S15) taking into account three magnetic order: paramagnetic (PM, *i.e.* no net magnetization and no atomic spin), ferromagnetic (FM, net magnetization and spin aligned in the same direction) and antiferromagnetic (AFM, no net magnetization but spin aligned in opposite

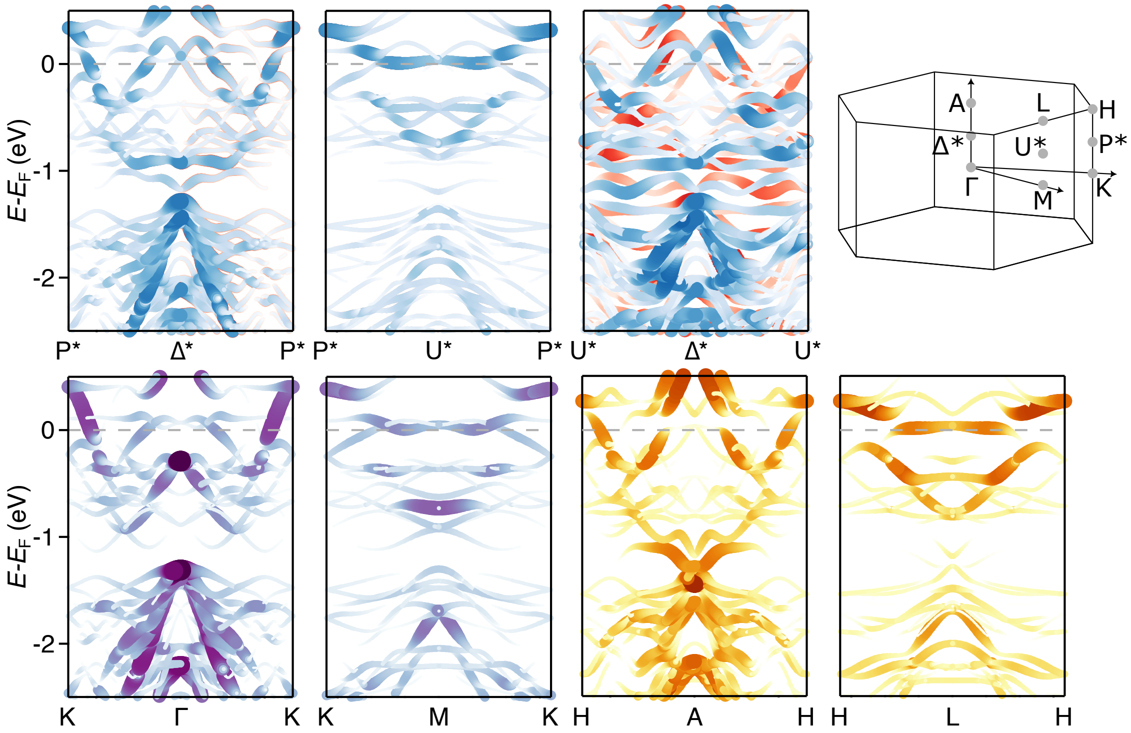

FIG. S14. **$Co_{1/4}NbSe_2$ energy versus momentum spectra along Γ–K calculated by DFT.** To complement the calculated band structure in the Γ-M direction of the main text, we present the calculated electronic structure in the Γ–K direction in addition to thecorresponding spectra at different positions in k_z as shown in the three-dimensional Brillouin zone.

Configuration	a (Å)	c (Å)	Total energy/Nb (eV)
01	7.06	12.38	0.277
02	7.06	12.40	0.223
03	6.93	12.32	0.000
04	6.95	12.34	0.043

TABLE S1. In-plane (a) and out-of-plane (c) relaxed lattice parameters, as well as total energy per Nb atom, for each configuration of paramagnetic Co intercalated 2×2 NbSe2. We set to 0 the most energetically favorable configuration.

directions) (Fig. S16). Results are summarized in Tab. S2. We find that the system stabilizes an AFM spin configuration and that the Co atoms are aligned on top of each other. In the main text we than proceed to show electronic band structure and fermi

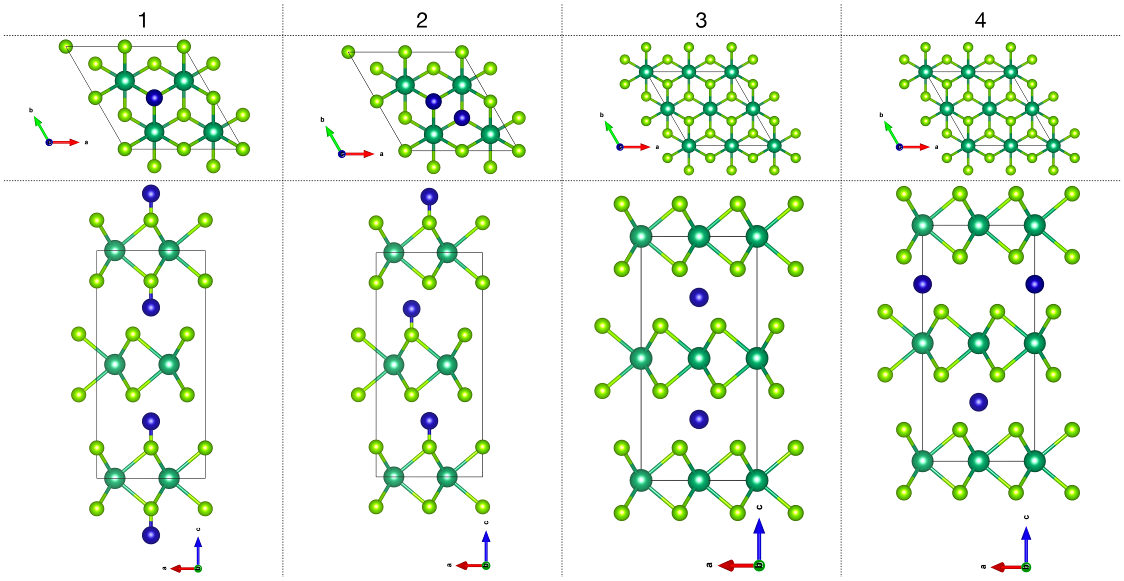

FIG. S15. **Possible configurations of $Co_{1/4}NbSe_2$.** Stick-and-ball models (top and side views) of possible configurations of $Co_{1/4}NbSe_2$ analised in DFT calculations. Dark (light) green spheres are Nb (Se) atoms, while blue spheres are Co atoms.

	Configuration	a (Å)	c (Å)	Total energy/Nb (eV)
AFM	03	6.96	12.44	0.0
	04	6.96	12.51	28.1
PM	03	6.93	12.32	15.2
	04	6.95	12.34	58.6
FM	03	6.94	12.35	13.9
	05	6.97	12.50	26.9

TABLE S2. In-plane (a) and out-of-plane (c) relaxed lattice parameters, as well as total energy per Nb atom, for most favorable $Co_{1/4}NbSe2$ intercalations in the antiferromagnetic (AFM), paramagnetic (PM) and ferromagnetic (FM) configurations. We set to 0 the most energetically favorable PM configuration.

surfaces calculations with the AFM - 03 structure however, since we show that Kramer degeneracy is lifted in points of the Brillouin zone which are not high-symmetry points, we call it altermagnetic (ALM).

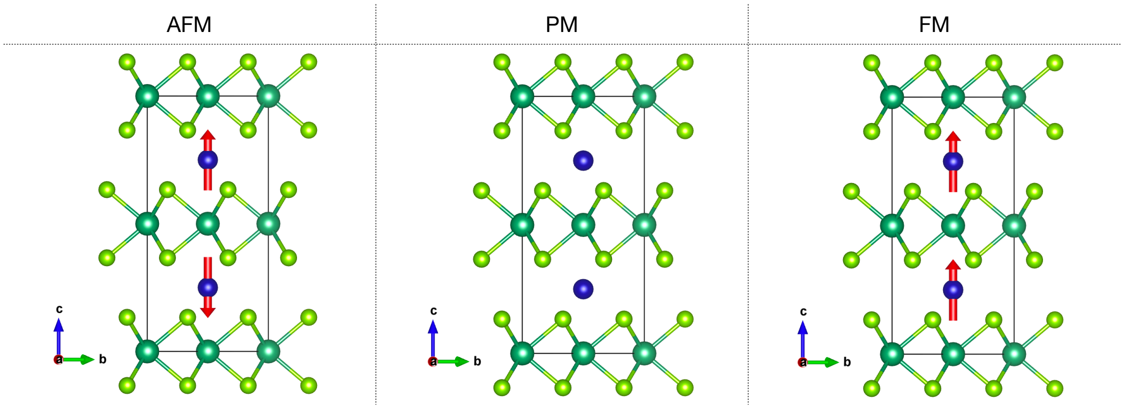

FIG. S16. **Spin configurations of $Co_{1/4}NbSe_2$.** Stick-and-ball models of possible spin configurations of the most energetically stable $Co_{1/4}NbSe_2$ analised in DFT calculations. Dark (light) green spheres are Nb (Se) atoms, while blue spheres are Co atoms.

[1] M. Bianchi, P. Hofmann, S. V. Hoffmann, N. C. Jones, Z. Li, J. A. Miwa, S. P. Møller, J. S. Nielsen, H. D. Thomsen, S. Ulstrup, and T. Worm, Status and strategy at isa, centre for storage ring facilities, aarhus university, denmark, The European Physical Journal Plus **138**, 132 (2023).

[2] A. Jones, P. Majchrzak, K. Volckaert, D. Biswas, J. Andersen, S. Hoffmann, N. Jones, Z. Jiang, Y. Chen, M. Jensen, R. Stenshøj, M. Bianchi, P. Hofmann, S. Ulstrup, and J. Miwa, A spatial- and angle-resolved photoemission spectroscopy beamline based on capillary optics at astrid2, Accepted to Review of Scientific Instruments (2025).

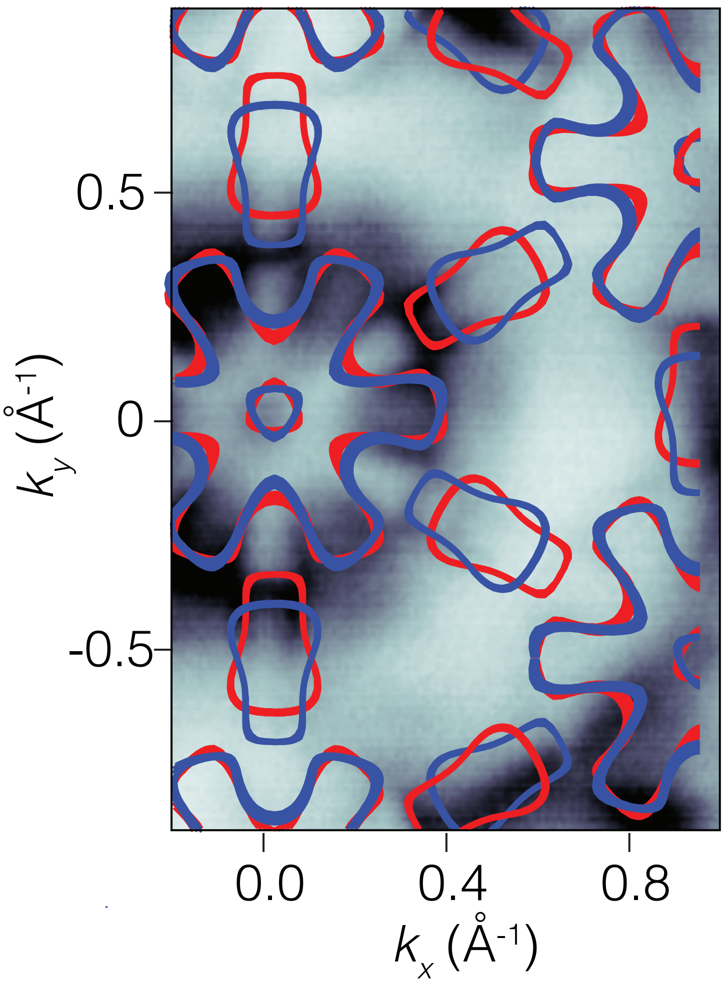

FIG. S17. **ARPES Fermi surface and calculated DFT.** ARPES data have been overlaid to the DFT calculated structure. Both are considered for $k_z = 0.25$; red and blue colors of the DFT indicate spin up and down respectively, and black indicates high intensity in the ARPES scale.